

RICE UNIVERSITY

**High Resolution Sculpting and Imaging of
Ultracold Neutral Plasmas**

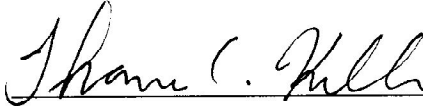
by

Patrick McQuillen

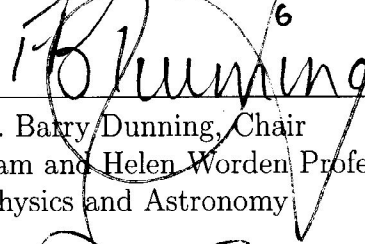
A THESIS SUBMITTED
IN PARTIAL FULFILLMENT OF THE
REQUIREMENTS FOR THE DEGREE

Master of Science

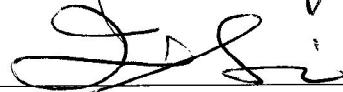
APPROVED, THESIS COMMITTEE:



Thomas C. Killian, Vice-Chair
Professor of Physics and Astronomy



F. Barry Dunning, Chair
Sam and Helen Worden Professor of
Physics and Astronomy



Qimiao Si
Harry C. and Olga K. Wiess Professor of
Physics and Astronomy

Houston, Texas

April, 2012

ABSTRACT

High Resolution Sculpting and Imaging of Ultracold Neutral Plasmas

by

Patrick McQuillen

The sculpting of ultracold neutral plasmas represents a frontier in the experimental study of collective modes in strongly coupled plasmas. By extending the range of accessible length scales to less than tens of microns we gain access to a regime where strong coupling's effects are predicted yet largely untested. To this effort, high resolution optical systems were designed, bench tested and implemented for sculpting and imaging ultracold neutral plasmas. Many complications and unexpected effects were documented to assist future experimental design considerations, including, those due to saturation and optical thickness, both of which limit the utility of 461 nm push beam modulations. It was concluded that sculpting should be performed on the 412 nm ionizing beam and real-time density space analysis is reliable for spatial frequencies up to 5 cyc/mm by using 4X magnified imaging. Higher spatial frequencies benefit from velocity space analysis due to extremely fast dynamics and low intensity levels.

Acknowledgments

Composing a list of people that have assisted this work, either directly or indirectly, is an intractable task. In order to avoid any unfortunate omission, I want to broadly speak to everyone that has made this possible, however do not let that detract each individual's significant contribution. A sincere thank you goes to all the past and present members of the Killian group for their hard work, great ideas, and endless motivation, I am proud to be part of such a fine research team. Behind that team, is a great school. I'd like to thank the entire Rice University family, for creating such a special place, where science flourishes while everyone has fun. I have thrived thanks to the school's unique environment.

Rice only represents the most recent stage of my life, a journey which started long ago. For this entire life of learning, I whole-heartedly thank my teachers, whom include, my friends, my family and even complete strangers. The experiences we've shared, have shaped me into who I am today. Finally, I'd like to thank our funding organizations, but not by simply listing their names, instead I vow to uphold their objectives and to carry on for the greater good of science and humanity.

Contents

Abstract	ii
Acknowledgments	iii
List of Illustrations	vi
List of Tables	viii
1 Introduction	1
1.1 Motivation	1
1.2 Collective Modes	2
1.2.1 Small Scale Collective Modes	2
1.3 Ultracold Neutral Plasmas	3
1.3.1 Experimental Details	3
1.4 Thesis Goals	6
2 Sculpting Ultracold Neutral Plasmas	8
2.1 Sculpting Density Modulations	8
2.2 Measuring Optical Resolution	8
2.3 High Resolution Sculpting	11
2.3.1 Optical Relay Design	11
2.3.2 Bench Testing Ionizing Relay	16
2.3.3 Reducing Inner Chamber Reflections	20
3 Imaging Ultracold Neutral Plasmas	22
3.1 ICCD Technology	22
3.2 High Resolution Imaging	25

3.2.1	Microscope System Design	25
3.2.2	Bench Testing Imaging Systems	27
3.2.3	CTF Calculated from ESF	29
4	System Contrast	33
4.1	Alignment	33
4.2	461 vs 412	38
4.2.1	Intensity Effects	38
4.2.2	Rescattered Light	41
4.3	Total System Performance	43
4.3.1	Velocity Space Analysis	50
4.4	Conclusion	52
A	Labview Overhaul	54
B	Matlab Standardization	56
B.1	Analysis Template	56
B.2	Matlab Defaults	56
B.2.1	startup.m	56
C	ESF - LSF Code	58
	Bibliography	67

Illustrations

1.1	Plasma Types in Temperature vs Density Phase Space	4
1.2	Previous Experimental Setup - Ionizing and Imaging Systems	5
1.3	Evolution of UNP After Formation	6
2.1	Typical CTF Measurement	10
2.2	Simulated Performance of Ionizing Relay	15
2.3	Focused Ionizing Relay Image of 1951 USAF Target	16
2.4	Ionizing Relay Bench Test Images	18
2.5	Ionizing Relay Performance Summary	19
2.6	Minimum Edge Depth vs. Field Depth	20
3.1	Intensified CCD Schematic	23
3.2	Point Spread Function of PI-MAX2 Intensified CCD	24
3.3	New Experimental Setup - Ionizing and Imaging Systems	26
3.4	Imaging System CTF Measurements	28
3.5	Subsampled ESF/LSF Measurement Process	31
3.6	CTF Calculated from ESF	32
4.1	Rotational Alignment of Mask	34
4.2	Alignment Sensitivity at 10 cyc/mm	36
4.3	Alignment Sensitivity at 20 cyc/mm	37
4.4	Saturation of 461 Push Beam, Effects on CTF	39

4.5	Ionization Fraction vs. 412 Ionizing Intensity	40
4.6	Density Effects on CTF of 20 cyc/mm Push Beam Modulations	42
4.7	Contrast vs. Optical Depth of 1 mm Gap	43
4.8	On Resonance Plasma Fluorescence with 3 cyc/mm Modulations	45
4.9	On Resonance Plasma Fluorescence with 5 cyc/mm Modulations	46
4.10	CTF of 5 cyc/mm Plasma Modulations vs. Detuning of Imaging Beam	47
4.11	CTF of 3 cyc/mm Plasma Density Modulations	48
4.12	CTF of 5 cyc/mm Plasma Density Modulations	48
4.13	Shifting of Plasma Fluorescence with Image Detuning	49
4.14	CTF of 10 cyc/mm Plasma Density Modulations	50
4.15	Velocity Distributions of Modulated UNPs	52

Tables

2.1	1951 USAF Resolution Target Specifications	17
4.1	Modulated Plasma Imaging Performance Results	47

Chapter 1

Introduction

1.1 Motivation

Collective behavior is truly a fundamental concept in plasma physics. Indeed, Chen defines a plasma as “a quasineutral gas of charged and neutral particles which exhibits collective behavior” [1]. Arising from the complex interaction of many long range Coulomb forces, collective phenomena are extremely diverse and have been studied extensively in traditional, ideal plasmas [2, 3]. This work represents a major extension of experimentally accessible collective mode studies in a strongly coupled or non-ideal plasma [4], where temperatures are low enough that discrete interparticle collisions are no longer hidden by a large thermal background and a slew of interesting phenomena have been predicted and seen [5, 6, 7]. The strength of this interparticle coupling is characterized by the strong coupling parameter, $\Gamma > 1$, determined by the ratio of Coulombic potential energy to temperature,

$$\Gamma = \frac{e^2}{4\pi\epsilon_0 a} \frac{1}{k_B T_E} \quad (1.1)$$

where, e is the fundamental unit of charge, a is the Wigner-Seitz radius or average interparticle spacing for a given density, ϵ_0 is the vacuum permittivity, k_B the Boltzmann constant, and T_e is the temperature of the electrons. Strong coupling represents a relatively unexplored regime, and challenges many of the fundamental plasma assumptions, calling for the development of new theories [8, 9]. Furthermore the physics is reflective of other strongly coupled systems that are not so experimen-

tally accessible due to extreme density and energy scales, like those created in inertial confinement fusion experiments and at the core of Jovian type gas giants [10].

1.2 Collective Modes

Though the general study of collective modes, is very rich and complex, our unmagnetized plasmas support only two electrostatic waves and we shall focus on these. Electrostatic waves are such that the inherent \mathbf{E} -field is parallel to the wave vector \mathbf{k} . Without an external \mathbf{B} -field they take two forms: high-frequency electron plasma oscillations and low-frequency ion acoustic waves. IAWs are sound-like for small \mathbf{k} and dispersionless for large \mathbf{k} . Electron plasma oscillations are the opposite. Specifically, the dispersion relation for IAWs is,

$$\frac{\omega}{k} = \sqrt{\frac{k_B T_e / m_i}{1 + k^2 \lambda_D^2}}, \quad (1.2)$$

where m_i is the ion mass and λ_D is the Debye length, to be covered in Section 1.2.1.

In a sense, understanding collective modes provides a decomposition of possible bulk behavior, they contribute greatly to the understanding and calculation of plasma transport properties as well as plasma instabilities [11, 12, 13, 14, 15]. The later of which is the typical limiting factor in plasma creation and confinement.

1.2.1 Small Scale Collective Modes

Theoretical constructs in plasma physics are founded upon a hierarchy of length and time scales. One such length scale is known as the Debye length and it describes the decay length of a test charge's \mathbf{E} -field, in the plasma. For a singly ionized, quasineutral plasma with $T_e \gg T_i$ the Debye length is,

$$\lambda_D \cong \sqrt{\frac{\epsilon_0 k_B T_e}{n e^2}}, \quad (1.3)$$

where $n \approx n_e \approx n_i$ is the local density of ions or electrons. The Debye length not only sets the scale for transition to dispersionless electrostatic waves (see Equation 1.2) but also the onset of Landau damping, i.e. when, $|\mathbf{k}|\lambda_D \approx 1$ [16]. This motivates our effort to excite and diagnose high resolution collective modes with spatial frequencies of at least 20 cyc/mm, for experimentally accessible $\lambda_D \approx 3 \mu\text{m}$ to $30 \mu\text{m}$.

1.3 Ultracold Neutral Plasmas

Created with atomic physics techniques, ultracold neutral plasmas provide extremely pure systems with incredible control over creation and diagnostic techniques [17, 18]. They are orders of magnitude colder than traditional plasmas which leads to their strongly coupled nature, $\Gamma_{ion} \approx 2-5$ after equilibration [19, 20, 21]. Furthermore, the use of strontium provides a convenient optical transition at 422 nm for both absorption and fluorescence spectroscopy [22, 23].

Ultracold neutral plasmas provide a great opportunity to probe collective modes in the exotic strongly coupled regime, thanks to their unique position in phase space, see Figure 1.1. Other strongly coupled plasmas depend on very high, typically solid densities to reach $\Gamma > 1$, which results in dynamics on femtosecond time scales and interatomic spacings of < 100 nm. Meanwhile UNPs, thanks to their relative low densities of 10^9 cm^{-3} , evolve on time scales of 100s of nanoseconds and have micrometer length scales. That is, UNPs offer an exploration of the same novel physics but with superb experimental accessibility to diagnostics and control.

1.3.1 Experimental Details

Our experiments start with a magneto optical trap (MOT) of ^{88}Sr atoms, operating on the dipole allowed fundamental transition, $^1\text{S}_0 - ^1\text{P}_1$ at 461 nm. We routinely cap-

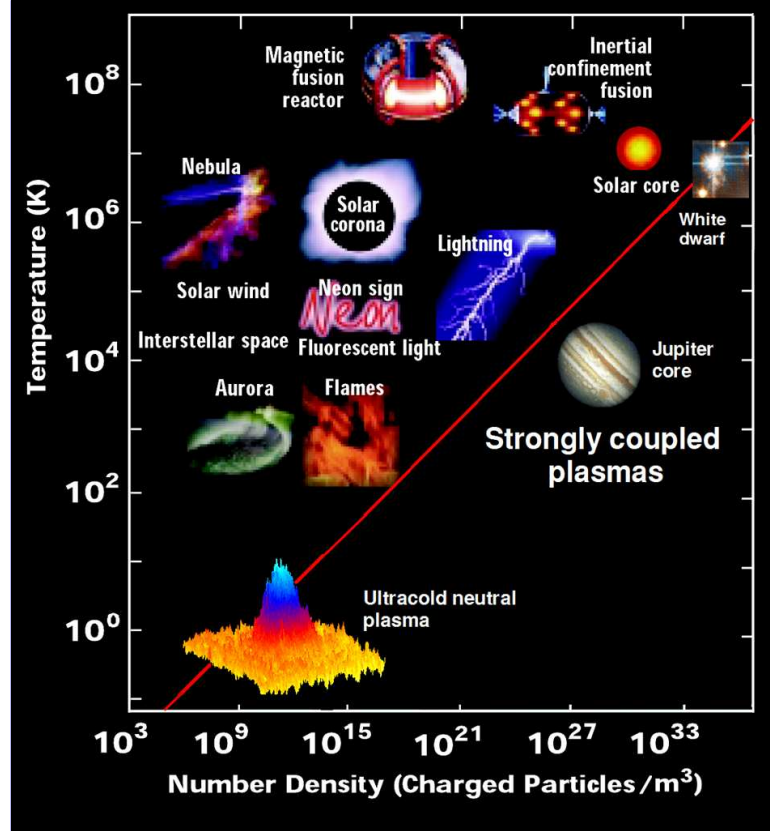


Figure 1.1 : Various types of plasmas and their position in temperature-density phase space, highlights UNPs exotic nature. The red line indicates the boundary of strong coupling, i.e. $\Gamma = 1$. Adapted from [18]

ture 200M - 500M atoms in a spherical Gaussian cloud, $n(r) = n_{atoms} \exp(-r^2/2\sigma_{cloud}^2)$ where $\sigma_{cloud} \approx 1.5$ mm and $n_{atoms} \approx 10^{15} \text{ m}^{-3}$ is the peak atom density. Atom temperatures are typically 7 mK.

The MOT cloud is then partially ionized by a two-photon process, which come from what we shall call the push and ionizing beams. The push beam is derived from the MOT laser system using the first order of an acoustic optical modulator (AOM), amplified by a Nd:YAG pumped Bethune cell [24], and used to excite atoms to the

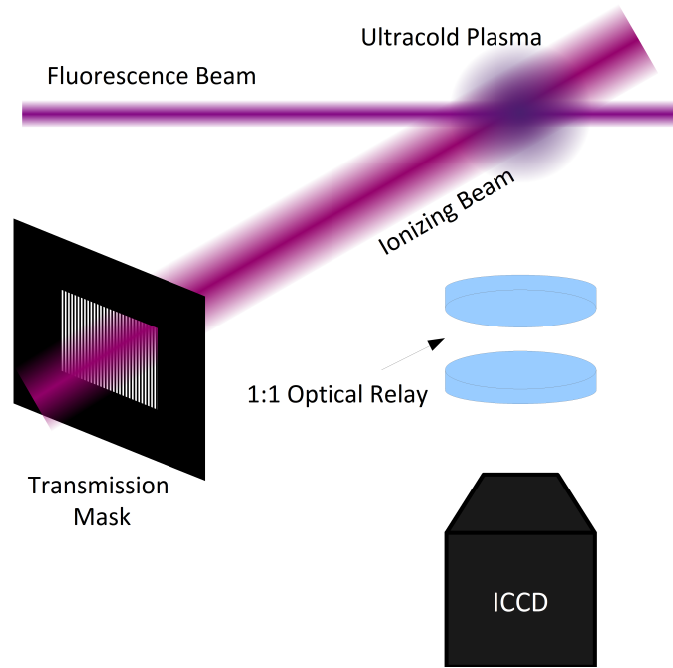


Figure 1.2 : Schematic of experimental configuration, shows previous ionizing and ion fluorescence imaging systems

1P_1 state. The ionizing beam is a 10 ns pulse from a pulse dye laser at 412 nm, so that each photon has just enough energy to liberate a single electron from its excited state, resulting in 10-70% ionization fraction (IF), dependent on intensity. Due to the large mass ratio of the ion to electron, the electron carries away most of the excess photon energy and thus the electron temperature is set by the ionizing wavelength (typically 25 K to 200 K with ≈ 1 K resolution, due to laser linewidth). Assuming the push beam and ionizing beams are uniform over the atom cloud, the ion density distribution follows that of the MOT. If we spatially modulate either intensity we control the local ionization probability and thus the initial density distribution of the UNP. Previous experiments, exploring ion acoustic waves, were accomplished by simply inserting a transmission mask into the ionizing laser [25], however as the

length scale of interest is decreased, diffraction effects, between the mask and the atoms, begin to limit the achievable contrast [26], this is precisely the issue addressed by this work.

Upon ionization of an unperturbed spherical plasma a series of interesting processes take place, see Figure 1.3 [27]. Very quickly (≈ 10 ns) the electrons reach global equilibrium [17], the heavier ions then (≈ 1 μ s) go through disorder induced heating, where potential energy of the initial randomly distributed ions is minimized and results in ≈ 1 K ions [20, 19]. Then for ≈ 100 μ s the plasma hydrodynamically expands into the vacuum [28, 29], until it completely diffuses. It is during this final expansion stage that the following experiments are conducted. The evolution of the imprinted density perturbations is the subject of study in sculpted UNP experiments.

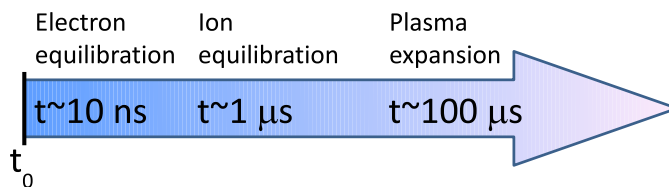


Figure 1.3 : Three distinct stages of plasma evolution. First, the electrons reach global equilibrium. Then ions reach local equilibrium and are heated by DIH. Finally, the plasma expands self similarly into the surrounding vacuum.

1.4 Thesis Goals

This thesis has two main goals, the design, implementation, and characterization of two optical systems: one for sculpting high resolution, high contrast density features into the plasma and another for imaging the resultant dynamics.

In order to circumvent contrast limitations imposed by diffraction as the mod-

ulated beam propagates from mask to atoms, an optical relay was designed to image the pattern onto the atoms with maximum fidelity [30], details of which are found in Chapter 2. This extends possible collective mode studies into the interesting $|\vec{k}|\lambda_D \cong 1$ regime, where Landau damping is expected. It also allows the sculpting of sharper, larger amplitude, non-linear density perturbations, such as large amplitude IAWs [31], or exciting shocks [32, 17] and maybe even solitons [33].

Imaging UNPs is constrained by two major considerations, the very low light levels of fluorescence imaging (approaching single photon) and the necessity for nanosecond gating, to time resolve dynamics. The only technology currently available to accommodate both of these issues simultaneously is the intensified CCD camera (ICCD). Unfortunately the major drawback of ICCD technology is poor spatial resolution, inherent to the complexity of intensifier design (explained in Chapter 3). To circumvent this limitation, a microscope setup was designed and implemented for magnifying the plasma image before the ICCD.

The processes of design and development, bench test results, and full system characterization follow in the proceeding chapters.

Chapter 2

Sculpting Ultracold Neutral Plasmas

2.1 Sculpting Density Modulations

Sculpted UNPs are created by spatially modulating the ionizing probability thus controlling the initial plasma density. In principle, this can be achieved with spatial filtering of either the push beam or ionizing beam by placing a transmission mask in the path of either beam [25]. However as the mask's spatial frequency increases, light's diffractive nature tends to blur mask features. The solution is to image the mask onto the atoms with an optical relay. To first order this can be accomplished with a simple spherical lens, but to achieve higher performance, additional considerations must be accounted for, these include, optical aberrations and alignment requirements [26]. Before we get too involved, we need to discuss some basic terminology and techniques for characterizing optical performance.

2.2 Measuring Optical Resolution

The task of quantifying resolution is not necessarily straightforward and is subject to arbitrary definitions and cut-offs. Despite manufacturers' tendencies to advertise a limiting resolution (LR), i.e. the highest spatial frequency for which an imaged bar pattern is discernible, the idea of a single number characterizing a system's resolution capabilities is flawed. Actual system performance varies as a function of spatial

frequency. One common measure for image quality is contrast,

$$C(\nu) = \frac{C_{Max} - C_{Min}}{C_{Max} + C_{Min}}, \quad (2.1)$$

where ν is the spatial frequency of interest, C_{Max} is the maximum signal level and C_{Min} is the minimum signal level. Since its value depends greatly on the object's characteristics we use it to define various transfer functions for particular periodic patterns. Perhaps the simplest pattern to consider is a periodic sine wave of a particular spatial frequency, ν , then the modulation transfer function (MTF) is defined as,

$$\text{MTF}(\nu) = 100\% * \frac{C_{sine}(\nu)}{C_{sine}(0)}. \quad (2.2)$$

Here $C(0)$ represents the contrast for very low frequencies and is necessary to normalize measurements, and $C(\nu)$ is the contrast calculated from maximum and minimum levels of the imaged sine wave.

The importance of the MTF is evident in the theoretical treatment of optical systems, for example, a multicomponent system's MTF is calculated by the product of the MTFs for each constituent piece. Many common optical elements (CCDs, simple lenses etc.) have analytically defined MTF curves [34] which are used to predict performance and design entire optical systems without ever tracing a single ray.

When it comes to actually testing an optical system, sinusoidal transmission masks are difficult to produce accurately and instead 50% duty cycle, binary square wave patterns (aka Ronchi gratings) are typically used to measure the contrast transfer function (CTF)[35],

$$\text{CTF}(\nu) = 100\% * \frac{C_{square}(\nu)}{C_{square}(0)}. \quad (2.3)$$

Figure 2.1 shows typical examples of CTF measurements.

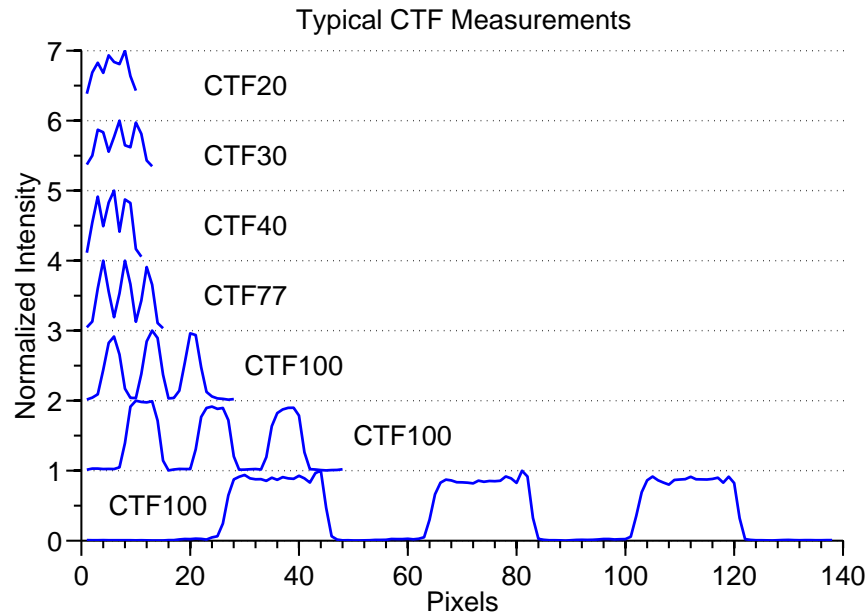


Figure 2.1 : Typical CTF measurements taken from images of a square wave pattern.

Fortunately Fourier taught us that a square wave is simply a series of sinusoidal waves, thus the MTF and CTF values can be related to one another, see Section 3.2.3 for details [36]. When considering CTF values, a note of caution is necessary, i.e. a CTF of 100%, doesn't indicate perfect reproduction. For example, see the bottom three measurements in Figure 2.1. MTF values do not suffer from this effect, and so they should be considered a more fundamental measure of optical performance. Standard shorthand notation writes $MTF = XX\%$ as MTFXX and similarly for CTF.

The concept of depth of field describes how the performance varies near the focal plane and it's value is entirely dependent on imaging needs. DOF is defined for a particular spatial frequency as the range of focal distances that give performance above a arbitrary minimum contrast. Intuitively, higher spatial frequencies or stricter imaging performance requirements lessens the DOF and vice versa.

2.3 High Resolution Sculpting

2.3.1 Optical Relay Design

With a goal of an optical relay capable of $> 50\%$ contrast at 20 cyc/mm over the majority of the depth of field (DOF) of the plasma ($\approx \pm 2$ mm) we consider the design process. The first step in optical design, is to identify basic system parameters using paraxial approximations. Paraxial ray tracing is a first order theory in which Snell's Law is simplified with the small angle approximation,

$$\frac{n_1}{n_2} = \frac{\sin(\theta_2)}{\sin(\theta_1)} \approx \frac{\theta_2}{\theta_1}, \quad (2.4)$$

here n is the index of refraction in medium 1 or 2, and θ is the ray's angle with respect to the surface normal. This approximation predicts perfect performance for spherical lenses and leads to the familiar optical formulas relating magnification (m), focal distance (f), image distance (s_1) and object distance (s_2).

$$\frac{1}{s_1} + \frac{1}{s_2} = \frac{1}{f} \quad (2.5)$$

and

$$m = \frac{s_2}{s_1} \quad (2.6)$$

For simplicity, we decided that the relay should be 1:1, i.e. $m = 1$. If optics are to be outside the vacuum chamber then access limitations were the first concern. Entering a $1\frac{1}{3}''$ viewport meant a clear aperture (CA) of diameter = $0.62''$ at an object distance, $s_2 = 4.6''$ from the atom cloud, giving us an maximum numerical aperture,

$$\text{NA} = \text{CA}/(2s) \approx 0.067. \quad (2.7)$$

Closely related is the minimum f-number,

$$f/\# = 1/(2\text{NA}) \approx 7.42. \quad (2.8)$$

Optical access also limits the minimum focal distance, $m = 1 \implies s_1 = s_2 \implies f = s_2/2 \implies f \geq 60 \text{ mm}$.

With knowledge of basic system parameters, next comes the selection of actual optics and characterization to ensure compliance with original design goals. The idea is to balance system performance against cost, the former is determined by a combination of the fundamental diffraction limit, aberrations (deviations from paraxial theory due to errors in the small angle approximation), manufacturing limitations, and system alignment.

The diffraction limit, is the maximum possible resolution of an optical system and it's precise definition requires an arbitrary criteria for saying two features are resolved. One common criteria is known as the Rayleigh criterion and it assumes that two separate point sources can be resolved when the center of one Airy disk (the diffraction transform of a point source) lies within the first dark band of the other's Airy disk. This leads to a smallest resolvable distance of

$$d = \frac{0.61\lambda}{\text{NA}}, \quad (2.9)$$

where λ is the wavelength of the light. For our maximum $\text{NA} \approx 0.067$ and $\lambda = 461 \text{ nm}$, we calculate a minimum Rayleigh diffraction limit of $\approx 4 \mu\text{m}$. When optics are of sufficient quality to reach this limit, we call them diffraction limited.

Aberrations are the deviations from paraxial optic's results due to errors in the small angle approximation. By including the next order term in the Taylor expansion of $\sin(\theta) \approx \theta - \frac{\theta^3}{3!}$, third-order theory identifies five primary monochromatic aberrations (spherical, astigmatism, coma, distortion and field curvature) all of which tend to blur the image. These were first studied in detail by Ludwig Von Seidel in the 1850s and are known as Seidel aberrations [37]. Their contributions are dependent on many system parameters and it is the task of the optical designer to minimize or

balance these aberrations for maximum overall performance. Conveniently, symmetric optical systems with magnification of unity do not suffer from coma or distortion, therefore we will only consider the other three.

The simplest solution for a 1:1 relay would be the spherical convex-convex lens. They are relatively easy to produce and therefore inexpensive, however they suffer greatly from spherical aberration (SA). With a minimum SA spot size given by, $0.134 * f / (f/\#)^3 \approx 20 \mu\text{m}$, this system would not be diffraction limited and we should look to more advanced, high-performance lenses.

Advanced lens designs come in three main varieties: multi element achromats, aspherical lenses, or GRAdient in the INdex of refraction (GRIN) lenses. Each design offers additional degrees of freedom to the designer for minimizing aberrations, at increased cost of course. An achromatic doublet, literally "a lens without color" is a two element lens, typically cemented together and chosen such that chromatic aberrations introduced by a negative element with high-index (flint), are corrected by the second positive low-index (crown) element. The dual element design is used to minimize on-axis spherical aberrations and coma and usually achieves diffraction limited monochromatic on-axis performance at infinite conjugate ratios. Achromatic triplets, designed for finite conjugate ratios also exist, though not in sufficiently long focal lengths for our needs.

To achieve better off axis performance, the next step is the aspherical (non-spherical) lens, in which aberrations are minimized for a particular conjugate ratio, by precise control over the surface curvature. These typically have the same diffraction limit for on axis performance but at a much higher cost due to complications in precision production of slightly non spherical surfaces. Their advantage is in their off-axis performance and becomes important in instances where beam quality and shape are

of utmost importance or you are concerned with accurately imaging far off axis field points. The two designs have been successfully combined and aspherized achromats are now being produced for large field, high resolution, color imaging. Finally, GRIN lenses use specially prepared glass with a varying index of refraction to the same effect but offer even more flexibility in design and the possibility of even better aberration correction.

To decide between these options we used OSLO (Optics Software for Layout and Optimization) by Lambda Research for modelling various designs of the ionizing relay. OSLO uses exact ray tracing to simulate performance, thus including all contributions from Seidel and higher order aberrations. From this point it was an iterative process of comparing calculated MTF curves for the various types of lenses available, starting cheap and moving up. We already decided a single convex-convex lens wasn't sufficient, so a dual element design with composite focal length of no less than 60 mm was explored. Commercial availability raised this lower limit to $f = 75$ mm but this resulted in a reflection, off the AR coated viewport, that was focused back onto the second (closest to chamber) lens causing significant damage. Hence the decision for $f = 200$ mm elements. With a NA imposed by the viewport window, and an object distance of 200 mm, a calculated CA of 1.1" suggests we use lenses larger than one inch diameter. The option of achromatic doublets simulated sufficient performance and a pair of Thorlab's 2" AC508-200-A doublets in a 1:1 conjugate ratio was chosen. Based on the simulated MTF curves from OSLO, Figure 2.2, we see $MTF > 75\%$ for 20 cyc/mm over the FOV necessary to encompass most (95%) of the plasma cloud, i.e. $\pm 2\sigma_{cloud} \approx \pm 3$ mm and diffraction limited performance, $MTF_{85} @ 20$ cyc/mm, for on-axis imaging.

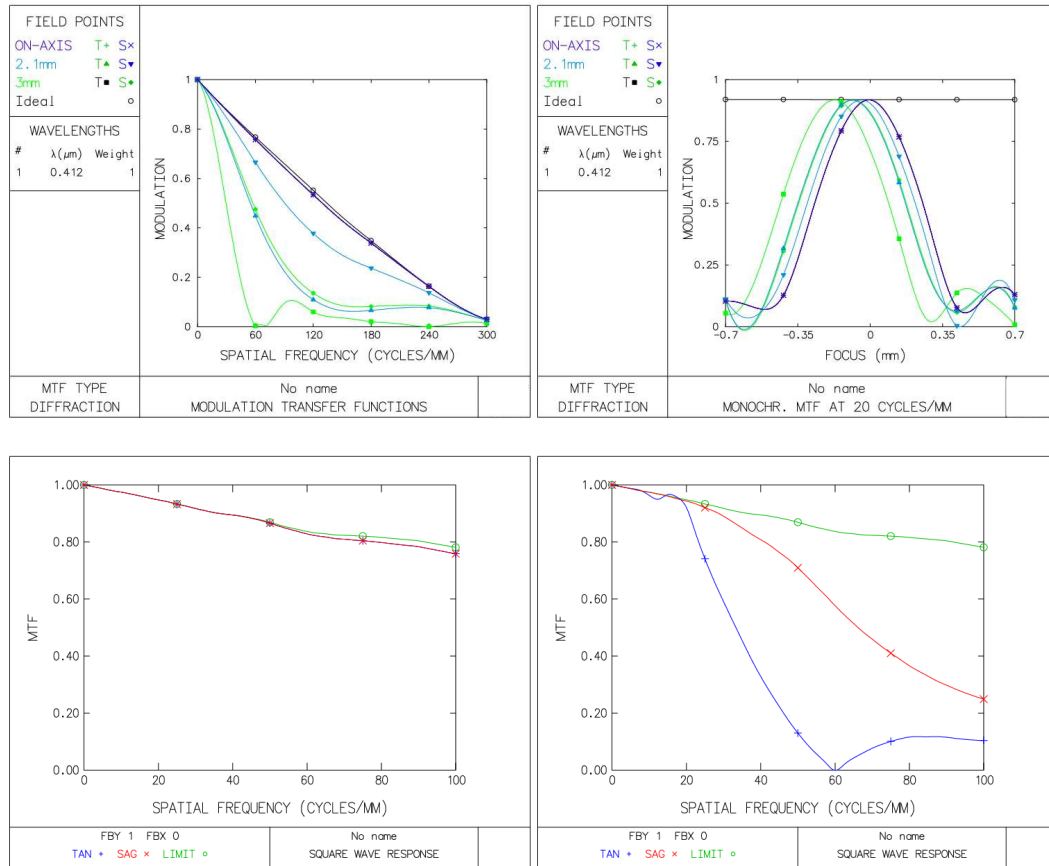


Figure 2.2 : OSLO's calculated performance for a pair of Thorlab's 2" AC508-200-A doublets in a 1:1 conjugate ratio. The MTF is calculated for various field points (upper left). On Axis, 2.1 mm off Axis and 3 mm off axis refer to radial distance from optical axis, in the object plane. T and S describe the orientation of the pattern. We typically image tangential (meridional) patterns while S are sagittal (radial) patterns. Ideal refers to the inherent diffraction limit and matches on-axis performance precisely, i.e. the relay is diffraction limited on-axis. MTF as a function of misfocus shows depth of field (upper right), note shift for various field points is due to field curvature. Simulated CTF performance, on axis (lower left) and at a 3mm field point (lower right), both show diffraction limited CTF out to 20 cyc/mm.

2.3.2 Bench Testing Ionizing Relay

A series of bench tests were conducted to measure CTF as a function of spatial frequency and image position. This was done by imaging a negative USAF 1951 resolution target (see Figure 2.3 and Table 2.1), back illuminated with 461 nm laser light, onto a PCO PixelFly Doubleshutter CCD. The camera position was adjusted so that the region of interest (ROI) was centered in the field of view (FOV) and a micrometer translation stage was used for fine control of camera position along the optical axis, i.e. focus. Images were captured over a range of camera displacements (± 1.6 mm, limited by stage travel), in order to explore the DOF, and can be seen in Figure 2.4.

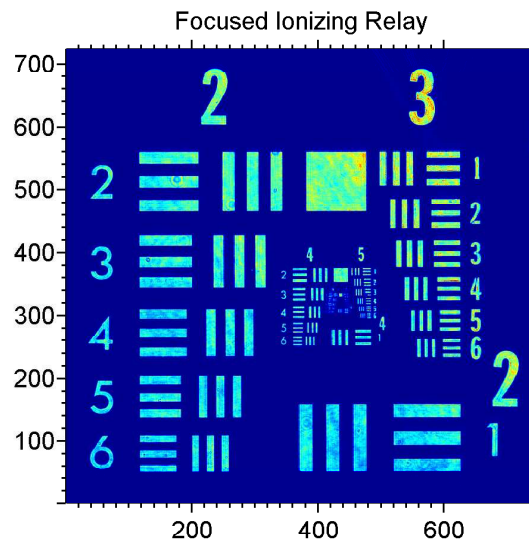


Figure 2.3 : In focus 1951 USAF Resolution target illuminated with 461 nm laser light and imaged with the new ionizing relay onto a PCO PixelFly Doubleshutter CCD

Table 2.1 : 1951 USAF Resolution Target [cyc/mm]

	Group					
Element	1	2	3	4	5	6
1	2.00	4.00	8.00	16.00	32.0	64.0
2	2.24	4.49	8.98	17.95	36.0	71.8
3	2.52	5.04	10.10	20.16	40.3	80.6
4	2.83	5.66	11.30	22.62	45.3	90.5
5	3.17	6.35	12.70	25.39	50.8	102.0
6	3.56	7.13	14.30	28.50	57.0	114.0

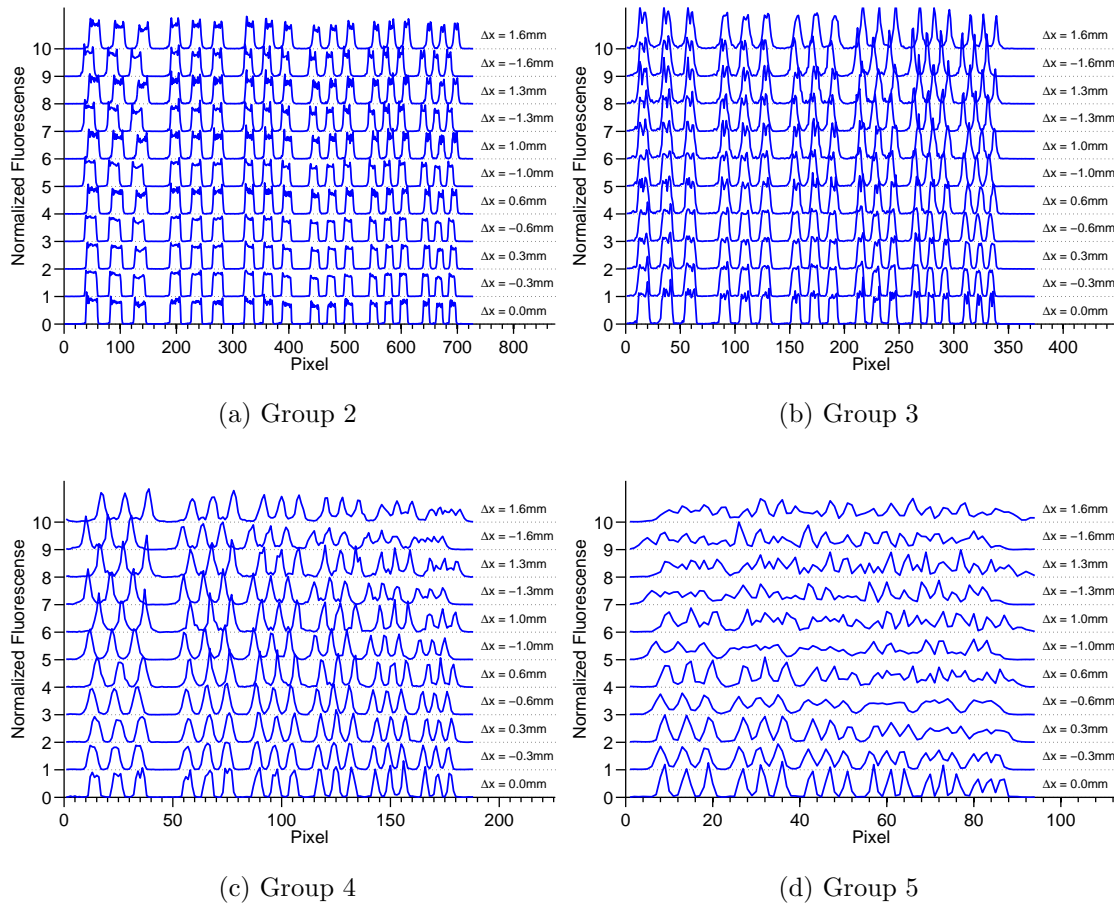


Figure 2.4 : Slices of relay imaged 1951 USAF target taken with PixelFly Doubleshutter CCD, (see Figure 2.3) used to measure CTF for various frequencies. Displacements on either side of focus explore DOF, which significantly surpasses simulated performance. Pixel size is $6.5 \mu\text{m}$ and panels (a)-(d) show 4-7 cyc/mm, 8-14 cyc/mm, 16-28 cyc/mm, and 32-57 cyc/mm, respectively.

As simulated the optical relay performed very well, way beyond our design goal of 20 cyc/mm. In fact bench tests of resolution were primarily limited by discrete sampling in the CCD. That is, CTF was near unity all the way to the Nyquist frequency, the highest spatial frequency resolvable by a discrete sensor, defined by,

$$f_{Nyquist} \equiv 1/2\Delta x, \quad (2.10)$$

where Δx is the pixel pitch or center to center spacing of the CCD pixels [$\Delta x = 6.5 \mu\text{m} \Rightarrow f_{Nyquist} \approx 77 \text{ cyc/mm}$ for the PixelFly Doubleshutter CCD, and $\Delta x = 13 \mu\text{m} \Rightarrow f_{Nyquist} \approx 38 \text{ cyc/mm}$, for the experiment's ICCD (Princeton Instruments PI-MAX2)].

Notice too that depth of field performance greatly surpassed OSLO simulations. We believe this is due to the coherent illumination by laser light.

To summarize these bench tests into a form convenient for conducting IAW type experiments the maximum resolution that was imaged with 100% contrast was determined, as a function of the desired DOF. The results are seen in Figure 2.5

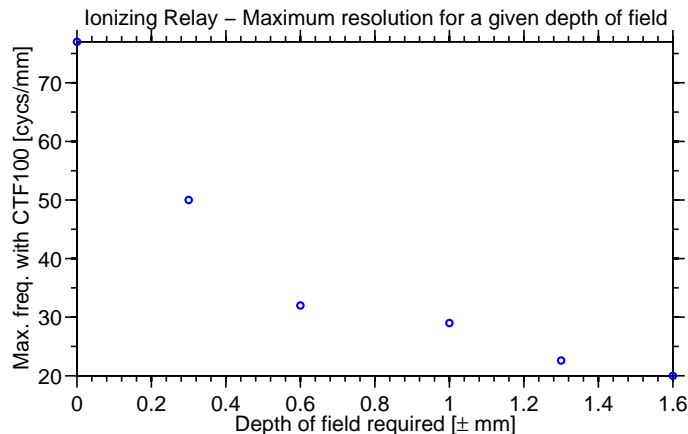


Figure 2.5 : Summary of ionizing relay performance. For a given depth of field the maximum resolution with CTF100 is plotted

Since we are also concerned with the sharpness of features that can be sculpted, we analyzed bench test results by fitting the edge of each bar in a slice of Group 2 to a finite width step function. Figure 2.6 shows the average width of that 100% amplitude step plotted vs. field depth, or misfocus.

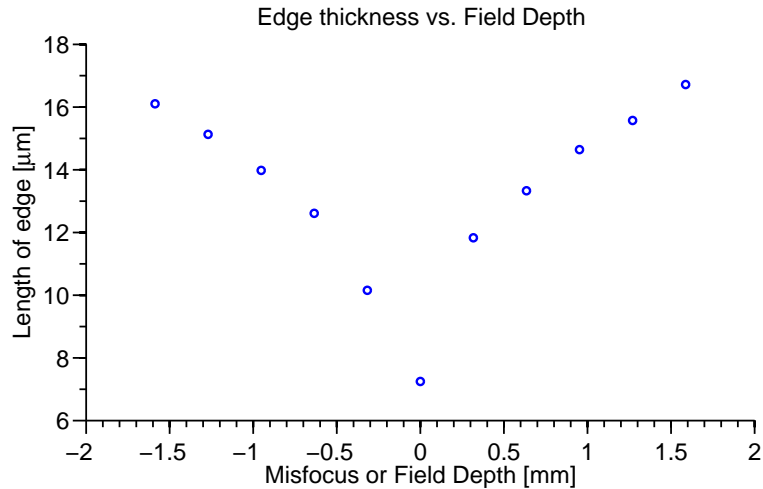


Figure 2.6 : Summary of ionizing relay performance. Edge thickness measurements taken from bench test images of 1951 USAF resolution target show an $\approx 7 \mu\text{m}$ transition, in the focal plane, and $< 16 \mu\text{m}$ transition over a depth of field of $\pm 1.6 \text{ mm}$. Note, in focus measurement is likely limited by CCD pixel size of $6.5 \mu\text{m}$ and in reality is closer to the diffraction limit of $4 \mu\text{m}$

2.3.3 Reducing Inner Chamber Reflections

Due to the optical relay, the sculpting beam is diverging after the plasma and does not clear the far chamber window. To catch and focus this beam down sufficiently to clear the chamber, a $f = 60 \text{ mm}$ plano-convex lens (Thorlab's PN LA1124-A) was installed 70 mm past the plasma using a groove grabber attachment and custom lens mount. This will catch all the light from up to a 12 mm diameter collimated ionizing

pattern, which is more than large enough to cover most UNPs. Furthermore, an iris was placed directly before the transmission mask to truncate the illuminated area and minimize unnecessary light in the chamber.

Chapter 3

Imaging Ultracold Neutral Plasmas

3.1 ICCD Technology

The previous imaging system consisted of an optical relay formed by a pair of Thorlab's 2" AC508-150-A doublets in a 1:1 conjugate ratio and a Roper Scientific, PI-MAX2 intensified CCD (ICCD). ICCDs are highly sensitive, i.e. can image a single photon and they provide unmatched gating speeds of 100s of femtoseconds. However their drawbacks are high cost (\approx \$20,000) and relatively poor resolution (\approx 40 μm spot size).

ICCDs are essentially an image intensifier tube coupled to a ccd camera. Originally developed for military night vision, image intensifiers use a series of stages (see Figure 3.1) to convert a single photon into a large electrical signal [38, 39]. When an incoming photon strikes the photocathode it has a chance (characterized as quantum efficiency) of liberating an electron. Then \approx 100 volts accelerates the electron towards a micro-channel plate (MCP). The MCP is a thin disc, a honeycomb of glass channels, each with a slightly conductive coating. With biasing (\approx 1 kV, and adjustable to control camera gain), the electron is accelerated through the MCP, creating a cascading shower of electrons, which strike a phosphorus screen. A fiber optic bundle couples the phosphor to a thermoelectrically cooled CCD, with minimal distortion and high efficiency. The resulting images are read out by integrated high speed electronics. Other designs include lens coupling to the ccd, with the advantage of being able to

remove the intensifier and with proper optics, better imaging performance.

The capability for fast gating is inherent to the design and requires no additional internal components. The Photocathode-MCP can be quickly biased on (off) to allow (prevent) liberated electrons to reach (from reaching) the MCP. The PI-MAX2 has a minimum gatewidth of 10 ns, for example.

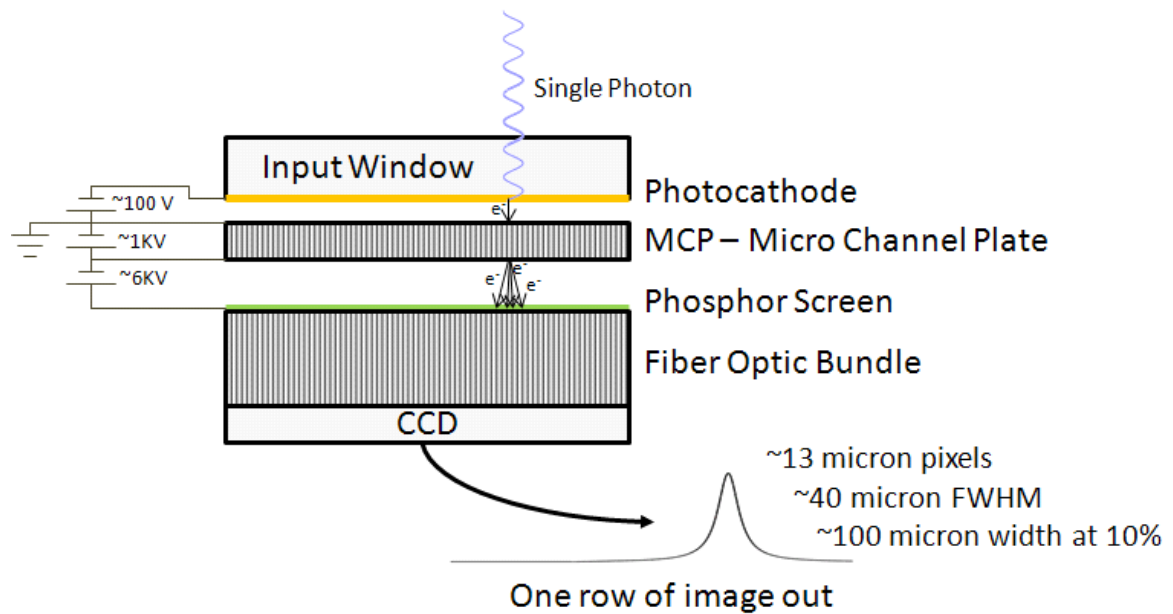


Figure 3.1 : Schematic of image intensifier. ICCD resolution or minimum image spot size is limited by many aspects of the total design: the MCP channel size, phosphor screen properties, physical dimensions, SNR, fiber bundle quality and CCD pixel size.

This process imposes many limits on the spatial resolution of an ICCD. In very low light levels, i.e. the photon counting regime, resolution is limited mainly by the signal to noise ratio (SNR) and secondarily by image spread or blurring [40, 41]. With relatively high light level ICCD spatial resolution is mainly limited by MCP channel size, optical coupling quality, and CCD pixel size [42]. The extent of this limitation

can be visualized with a measurement of the point spread function, (PSF - the image of a point source) see Figure 3.2. In essence this PSF completely characterizes the optical system and can be used to calculate the system's MTF, however the measurement is inherently noisy since the signal is essentially one pixel in a sea of background pixels, i.e. very low SNR.

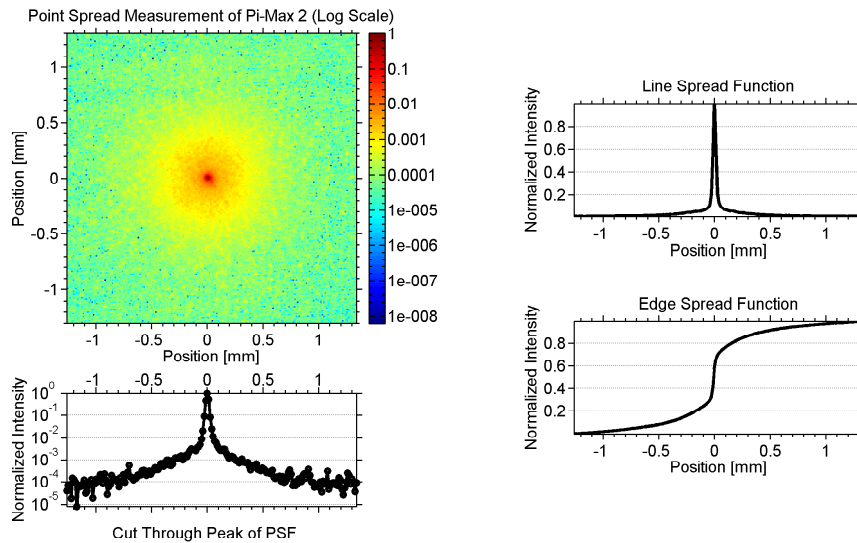


Figure 3.2 : Log scale image of the output face of a fiber optic cable, $\approx 6 \mu\text{m}$ spot (upper left). Notice the far reaching tail, which is responsible for diminished contrast, even at low spatial frequencies. A profile of the PSF shows the extent of the tail (lower left). If the PSF is integrated along one dimension it produces the line spread function (upper right) and the edge spread function is the antiderivative of the LSF (lower right).

The PSF allows calculation of the image intensity distribution, based on knowledge of the object's intensity distribution. Assuming optical performance is shift-invariant and distortion free, image intensity distribution, S_{image} , is the convolution of the

object's intensity distribution, S_{object} , and the optical system's PSF,

$$S_{image}(x, y) = \int_{-\infty}^{+\infty} \int_{-\infty}^{+\infty} S_{object}(x', y') PSF(x - x', y - y') dx' dy'. \quad (3.1)$$

Or in one dimension the LSF, is given by the following expression,

$$LSF(x) = \int_{-\infty}^{+\infty} PSF(x, y) dy, \quad (3.2)$$

which serves as the convolution kernel for 1D images,

$$S_{image}(x) = \int_{-\infty}^{+\infty} S_{object}(x') LSF(x - x') dx'. \quad (3.3)$$

Finally the edge spread function is given by,

$$ESF(x) = \int_{-\infty}^x LSF(x') dx', \quad (3.4)$$

and characterizes the system's response to a heavyside step function.

3.2 High Resolution Imaging

3.2.1 Microscope System Design

To overcome the inherent limitation of our ICCD camera, external optics were chosen to magnify the plasma fluorescence, see Figure 3.3. Again we first consider optical access considerations. A CA of 1.5" at $s_1 \approx 4.6$ " gives a maximum NA of 0.163 or $f/\# \approx 3.06$ which is preserved by the imaging relay with it's NA of 0.169 or $f/\# \approx 2.96$. The preexisting imaging relay was bench tested independently from the ICCD and determined to be sufficient, considering the frequencies of interest and the limitations of the intensifier. To maintain 1X imaging capabilities a Nikon 105 mm $f/2.8D$ AF Micro-Nikkor Lens was mounted to the front of the ICCD using Roper's f-mount adapter. The lens was set to maximum aperture, $NA = 0.179$, and focused

at the closest working distance, for a 1:1 conjugate ratio. Then the camera was moved away from the relay so that the image from the imaging relay was refocused onto the ICCD.

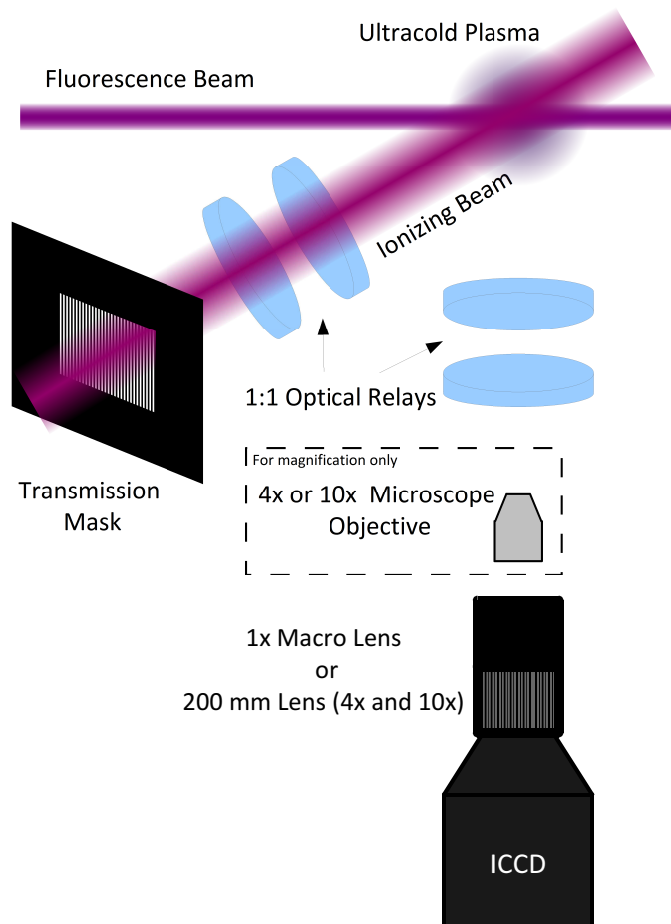


Figure 3.3 : Schematic of experimental configuration, shows ionizing and ion fluorescence imaging systems of 1X, 4X and 10X

Four and ten times magnification are accomplished with a combination of an Olympus Achromat Objective, either a 4X 0.10 NA, 18.5 mm WD (Thorlab's PN RMS4X) or a 10X 0.25 NA, 10.6 mm WD (Thorlab's PN RMS10X) and a Nikon AF-

S DX Zoom-Nikkor 55 mm to 200 mm f/4-5.6G ED zoom lens. Microscope objectives are typically designed to work in conjunction with $f = 200$ mm infinity corrected eyepieces, hence the choice of the Nikon zoom lens, which is set to $f = 200$ mm at maximum aperture, CA ≈ 35.7 mm and focused at infinity. Note that while the 1X and 10X systems are aperture limited by the vacuum chamber, the 4X system is limited by the 0.10 NA of the 4X objective. As such we expect a 65% decrease in collected fluorescence using 4X magnification. The 4X and 10X systems also decrease the intensity on the CCD by the square of their magnification, 1/16th and 1/100th, respectively, although pixel binning can compensate. So while the 4X greatly enhances resolution, it decrease the signal level of a single pixel to only 4% of that at 1X and correspondingly decreases the SNR. Single pixel SNR at 10X is 1% of that at 1X.

3.2.2 Bench Testing Imaging Systems

Bench tests of the imaging relay, ICCD camera, and new lens systems where accomplished similarly to the ionizing relay test as in Chapter 2, except that 422 nm light was used. Figure 3.4 shows the results. As expected from PSF measurements our system shows diminished contrast (CTF50) for intermediate frequencies (1-12 cyc/mm at 1X) which drastically diminishes perceived image quality despite the high limiting resolution (LR) of 30 cyc/mm [41, Figure 3]. When scaled by the inverse of their magnification factor, the 4X and 10X systems show similar performance for intermediate frequencies, however high frequency performance falls off faster than scaled 1X performance.

Since the plasma is an extended object, the DOF of the imaging system is important to consider. By compressing the fluorescence imaging beam in the vertical

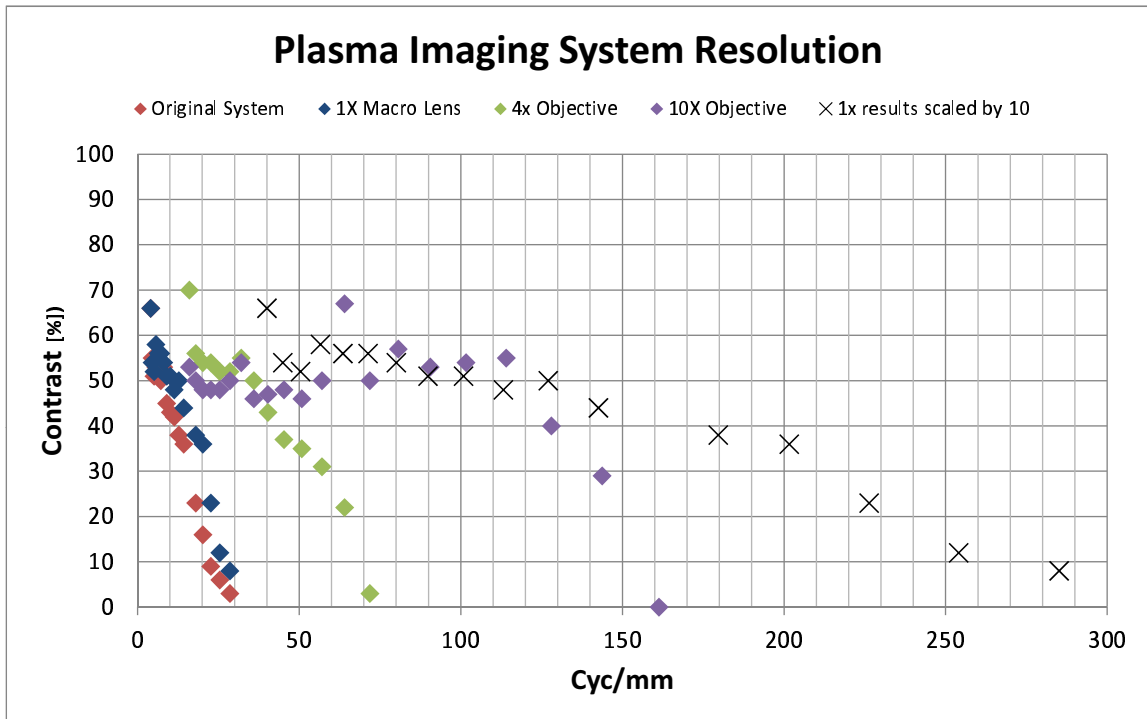


Figure 3.4 : Bench test measurements of CTF for all four versions of the imaging system: previous system, 1X macro, 4X and 10X magnification are plotted. In general performance scales with magnification, except that high frequency performance falls off faster for larger absolute spatial frequencies.

direction, we only excite fluorescence from a thin layer in the plasma and lessen the requirements for imaging system DOF. Currently the beam is shaped to have a vertical waist, $w_{vertical}$, of $\approx 200 \mu\text{m}$. Plasma imaging performance will be degraded by insufficient DOF unless the layer thickness is less than the DOF. Since DOF is a complex function of imaging requirements and spatial frequency, the proper image beam thickness is wildly dependent on experimental needs and should always be a consideration with high resolution imaging. Approximate measures of imaging DOF are provided in Figures 4.2 and 4.3. Again, precise values depend on arbitrary criteria

for acceptable contrast and depend on the spatial frequency of interest.

3.2.3 CTF Calculated from ESF

As an independent verification of the 1X system performance, we measured a sub-sampled edge spread function (SSESF) and calculated the MTF, with a slightly modified version of the algorithm developed by Buhr et. al. in 2005 [43, 44, 45]. For details see the code in Appendix C. Due to it's simplicity of calculating the entire MTF from one single image and it's proven accuracy, perhaps this method should be preferred for characterizing optical systems in the future.

The ESF is the image of a heavyside function, recorded by imaging the edge of a razor blade. Sub-sampling refers to the fact that images are recorded with a slight angle so that the true edge of the blade is slightly displaced for each neighboring row of pixels, see Figure 3.5. This provides subpixel size sampling of the edge image, i.e. spectral information beyond the Nyquist frequency. The derivative of the ESF is the line spread function (LSF), i.e. the image transform of a line source. The LSF is truncated at the previously measured extent of the PSF, by application of a Hamming window, ensuring far wings go to zero and minimizing FFT leakage in the next step. The MTF is calculate by a discrete fast Fourier transform of the LSF. Finally the CTF can be constructed by a series expansion known as the Coltman formula [36],

$$\text{CTF}(f) = \frac{4}{\pi} \sum_{k=1,3,5,7\dots} B_k \frac{\text{MTF}(kf)}{k}, \quad (3.5)$$

where B_k is

$$B_k = (-1)^{\frac{k-1}{2}}. \quad (3.6)$$

The resulting calculated CTF, agreed well with values measured from discreet bar patterns on the 1951 USAF Resolution target, see Figure 3.6. The noticeable dis-

crepancy can be explained by the fact that the Coltman formula assumes an infinite bar pattern and we used a 3-bar target. Inaccuracies on the order of +5% are typical on measured 3-bar targets when compared to true CTF values. [46, 47].

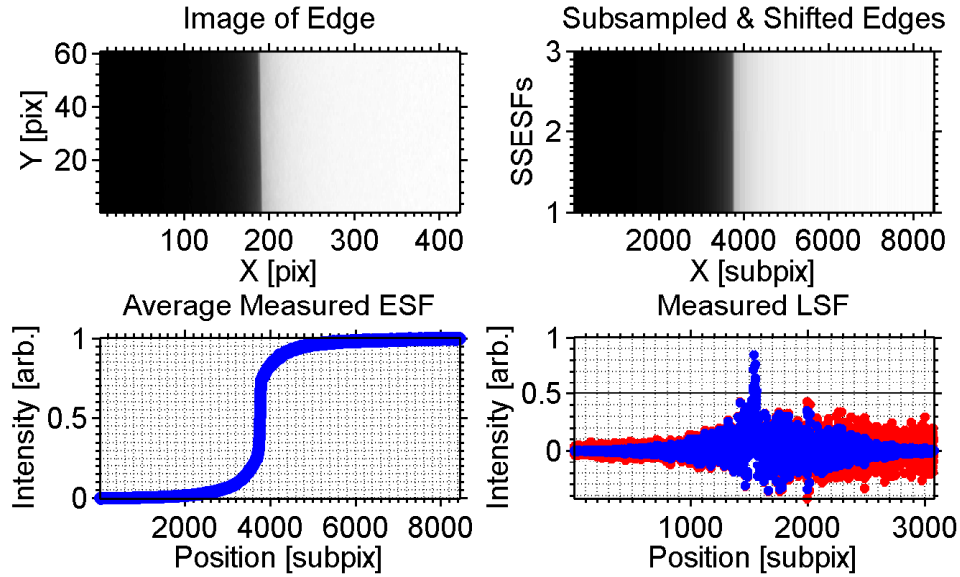


Figure 3.5 : (upper left) A razor blade was imaged at a small angle to provide sub pixel sampling of the edge. (upper right) Several sub-sampled edge spread functions (SSESFs) are created from a single image, and aligned in anticipation of averaging. (lower left) The averaged SSESF. (lower right) The derivative of the SSESF is the sub-sampled line spread function (SSLSF), which contains complete spectral response information well past the Nyquist frequency. This frame also shows the effect of applying the Hamming window to the SSLSF, (red LSF is reduced to the blue LSF) this is necessary to ensure far wings go to zero, impossible to experimentally measure due to noise.

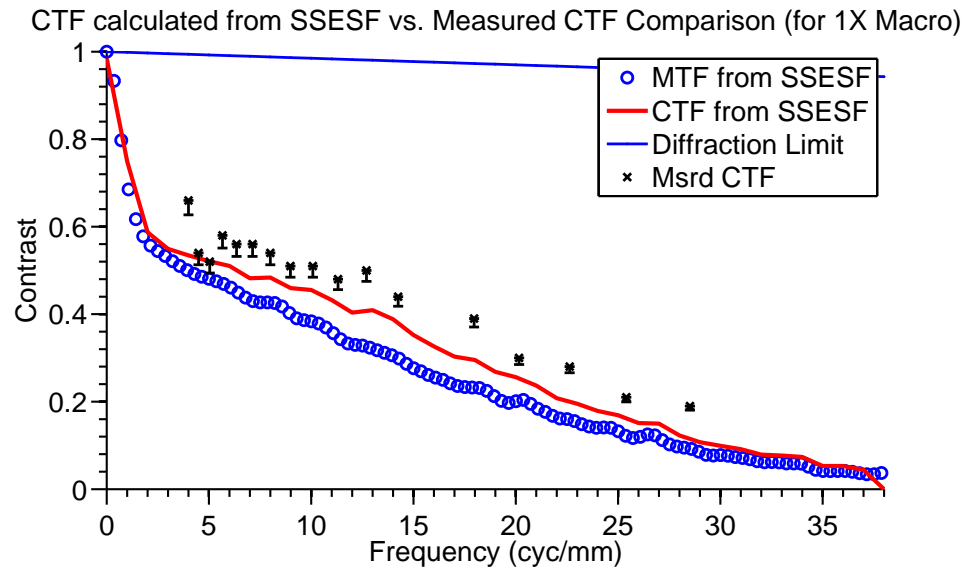


Figure 3.6 : Alternative methods confirm bench tests of 1X macro system. Subsampled ESF measurement calculated a CTF (red solid line) which agrees sufficiently well with directly measured CTF values (black x's), with errorbars indicating the $\approx 5\%$ discrepancy due to using a finite length 3-bar pattern. The intermediate stage of calculating MTF (blue o's) was also shown to highlight the difference between CTF and MTF values. The calculated diffraction limit is shown (solid blue line), the system is far from diffraction limited at 1X magnification.

Chapter 4

System Contrast

With understanding of the intensity pattern falling on the atoms and the capabilities of our imaging system, we were then ready to characterize the entire system. For a simple optical system the combined performance is simply the product of the individual MTFs, however there are effects in the atoms that must be considered carefully and we should consider bench test performance to be nothing more than an upper bound on total system performance.

4.1 Alignment

Both relays are constructed from rigid 2" lens tubing. The ionizing relay is attached directly to the outer diameter of a vacuum chamber window by means of a custom lens tube adapter, thus setting the proper relay-atom distance, when lens is flush with adapter. The imaging relay is mounted directly below the chamber with a 90° mirror between the two lenses. During bench test the imaging relay mirror was aligned so that a coaxial beam, exited the relay coaxially. Gross alignment of both relays is accomplished by centering them in their respective beams, which should be prealigned to be coaxial with a pair of opposing vacuum chamber windows. Using alignment guides on the lenses tubes and ensuring the beam is nearly undeviated in the distance, ensures sufficient first-order centering and alignment.

Next, there are four critical alignments that need fine control.

- Positioning of the mask, along the ionizing beam, is critical to placing the image plane directly in the center of the MOT and transverse alignment allows the pattern to shift relative to the overall cloud. This is accomplished with a standard 2 axis translation stage.
- The rotation of the mask must be precisely aligned so that the planes of plasma are parallel to the optical axis, see Figure 4.1. This is done with a high precision rotational mount.
- The imaging relay must focus it's image onto the object plane of the macro lens. This is accomplished by a fine threaded adjustable length lens tube.
- A XYZ translation stage is used in the magnification setups in order to position the objective so that it is focused and centered on the relayed image.

Since the 200 mm lens is focused at infinity for the microscope setups, the objective-zoom lens distance is unimportant.

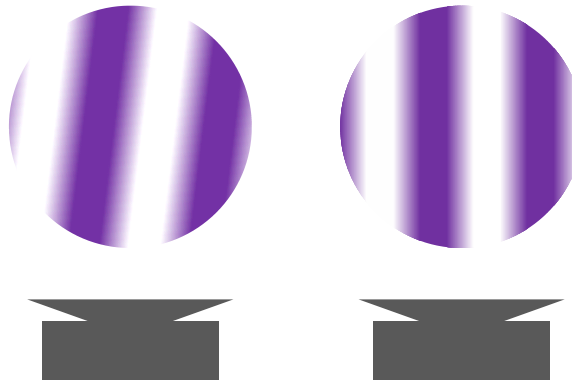


Figure 4.1 : Rotational alignment of the transmission mask is critical to ensure contrast is not diminished by poor line of sight.

To measure sensitivity to these alignments we performed resolution tests on atomic fluorescence. By modulating the push beam and imaging the fluorescence with the PixelFly camera we have a high resolution view of the intensity patterns on the atoms, as seen through the imaging relay, without the severe limitations imposed by the ICCD. This relies on the fact that the fluorescence intensity is proportional to actual push beam intensity, i.e. we must avoid saturating the transition (the push beam is unamplified for these studies). The effects of saturation will be discussed further in Section 4.2.1. Figures 4.2 and 4.3 show the results for 10 and 20 cyc/mm respectively. Note these do not represent maximum obtainable atom fluorescence contrasts since these measurements were taken before limiting effects of high density were discovered, to be discussed in Section 4.2.2.

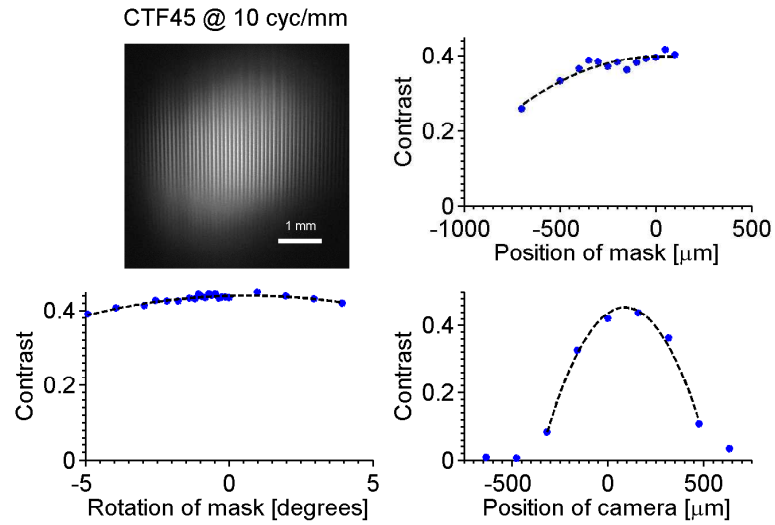


Figure 4.2 : CTF measurements were performed on push beam fluorescence at 10 cyc/mm to test sensitivity to mask position, mask rotation and camera position. Camera position sensitivity is directly related to imaging system DOF, however the measurement is broadened by the finite depth of the illumination sheet. The sheet thickness was set by manual tape masking and as such is on the order of 500 μm to 1000 μm , this means the DOF for any discernible contrast at 10 cyc/mm is on the order of a few 100 μm .

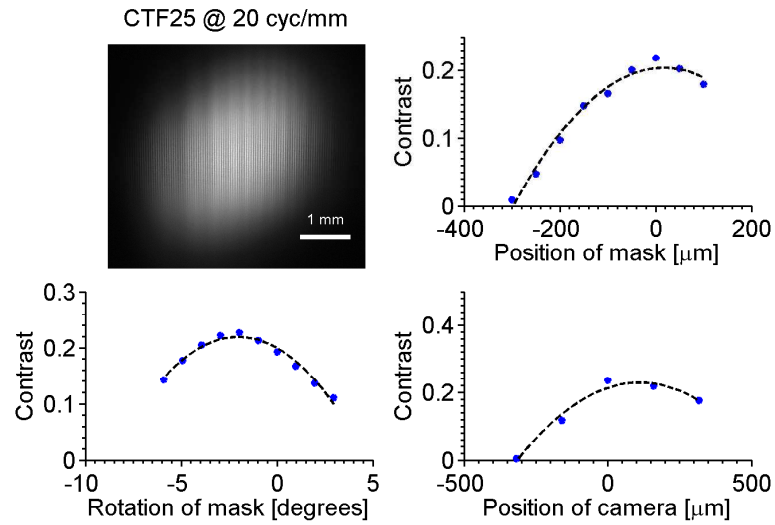


Figure 4.3 : CTF measurements were performed on push beam fluorescence at 20 cyc/mm to test sensitivity to mask position, mask rotation and camera position. Camera position sensitivity is directly related to imaging system DOF, however the measurement is broadened by the finite depth of the illumination sheet. The sheet thickness was set by manual tape masking and as such is on the order of 500 μm to 1000 μm , this means the DOF for any discernible contrast at 20 cyc/mm is on the order of a 100 μm .

4.2 461 vs 412

Sculpting UNPs can be accomplished by modulating either the 461 nm push beam or the 421 nm ionizing beam. We've seen how modulating the push beam is useful for testing performance of the ionizing relay system, however it is plagued by a few limitations that ionizing beam modulations avoid.

4.2.1 Intensity Effects

As previously mentioned, the push beam is amplified in a Bethune style dye cell in order to increase ionization fraction. By increasing the Rabi frequency way beyond a 10 ns π -pulse, amplification allows $> 50\%$ ionization fractions. The level of amplification for the push beam is easily adjustable by varying the pump power, and is based on experimental needs. Since atomic excitations saturate when $S_0 \equiv I/I_{sat} \gg 1$, too much amplification will diminish contrast. To explore this effect bench test results of the ionizing relay were normalized by actual intensities of the push beam, for various levels of amplification, see Figure 4.4. An unamplified push beam, of 9.5 mW with an $1/e^2$ -radius of 2.25 mm gives $S_0 \approx 2.6$, and shouldn't measurably effect contrast. However with the possible amplification of nearly 500X, the fully amplified push beam with $S_0 \approx 1330$ destroys all contrast, since the probability of excitation is nearly constant across the pattern. In summary the level of push beam amplification must be balanced between ionization fraction and contrast desired for 461 nm modulations.

To explore saturation of the 412 ionizing transition, we measured ionization fraction as a function of 412 intensity. The results are shown in Figure 4.5. Following the work of Burkhardt et. al. [48] we fit to Equation 4.1 and measure an absolute photoionization cross section of $\sigma_{PI} \approx 77$ Mb, which is comparable to measurements

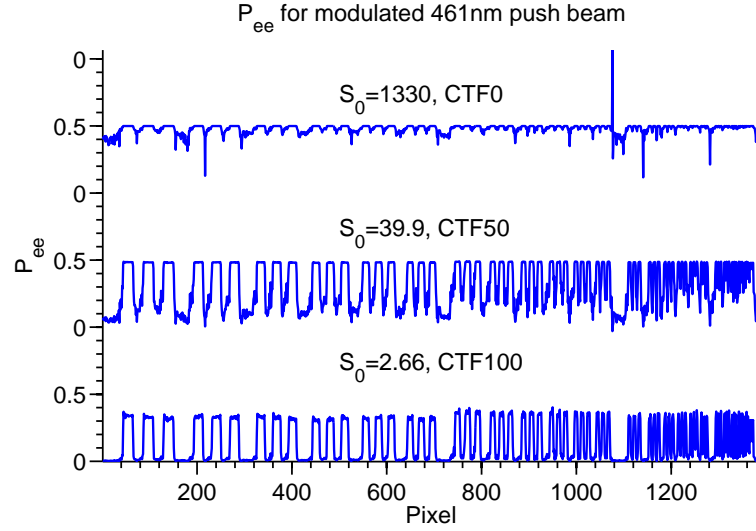


Figure 4.4 : All spatial frequencies are reduced to zero contrast for high intensity push beams. $S_0 = 1330$ corresponds to upper limit of amplification for current experimental setup. $S_0 \approx 40$ results in a near 50% reduction in contrast across all spatial frequencies. $S_0 = 2.6$ corresponds to the current unamplified push beam intensity.

by Mende et. al. [49].

$$N_{ion} = N_{exc} \left(1 - e^{-\frac{\sigma_{PI} U}{2\hbar\omega A}} \right), \quad (4.1)$$

where N_{ion} is the number of ions created, N_{exc} is the number in the excited 1P_1 state, U is the total energy per ionizing pulse, $\hbar\omega$ is the energy of one photon and A is the illuminated area and we assume $N_{exc} = N_{atoms}$ since the push beam transition is highly saturated. Since we typically operate in a fairly linear regime and the gaps of the pattern are truly dark we expect little effect on contrast due to ionizing saturation.

A different sort of intensity effect becomes important for the 412 ionizing beam, i.e. damage from unwanted reflections. Even a small percentage of the original pulse

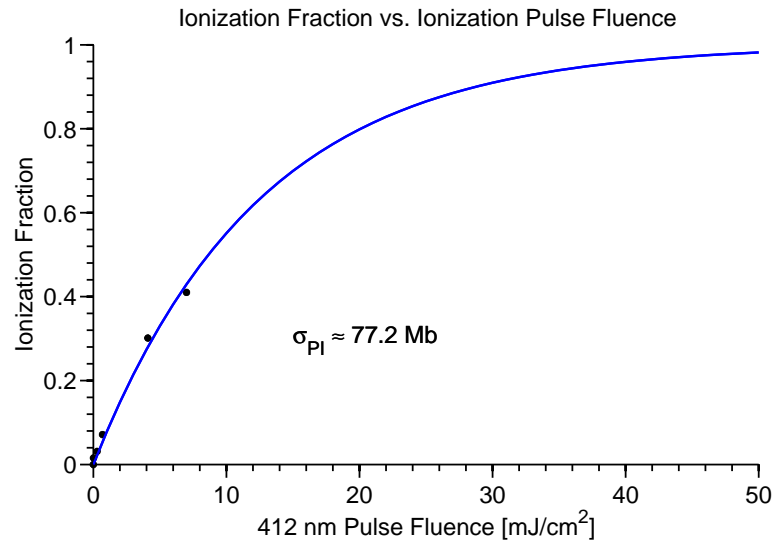


Figure 4.5 : Measured ionization fraction versus 412 nm beam intensity agrees with published values for photoionization cross section. For this measurement the 412 beam was expanded and sent through an iris so that only the central region ($\approx 1 \text{ cm}^2$) with nearly uniform intensity, was sent into the chamber.

energy is damaging if it is focused through one of the high quality achromats. An original design of the ionizing relay using $f = 150$ mm lenses was changed to $f = 200$ mm to avoid lens damage due to a focused reflection off the anti-reflection coated window. Also the spacing between lenses must be kept to a minimum to prevent the same with $f = 200$ mm lenses. Finally it was noted that if the lenses are installed backwards, with the highest curvature surfaces outward, then a reflection is focused back onto the target and damages the chrome mask.

4.2.2 Rescattered Light

Another limitation of contrast with push beam sculpting depends on the optical thickness or optical depth (OD) of the atom cloud. Understood as the probability of absorption for a photon travelling through a distance, L , through a the cloud of density, n .

$$\text{OD} = n * L * \sigma_{abs}, \quad (4.2)$$

where σ_{abs} is the absorption cross section given by [50],

$$\sigma_{abs} = \frac{3\lambda^2}{2\pi} \left[1 + \left(\frac{2 * \Delta}{\Gamma} \right)^2 \right]^{-1}. \quad (4.3)$$

Here, detuning, $\Delta = 20$ MHz and the natural linewidth of $\Gamma = 30.5$ MHz gives a $\sigma_{abs} = 3.9 \times 10^{-14} \text{ m}^2$.

An optically thick cloud has a significant probability of scattered photon absorption in unilluminated regions of the modulation patterns, subsequently decreasing achievable contrast. This was first noticed when a dependence on density was found for push beam fluorescence contrast at 20 cyc/mm, see Figure 4.6. To explore the effect more generally a large gap of 1 mm was imaged and contrast measured at various optical depths. Figure 4.7 shows the raw data, with contrast measurements and con-

firmly a reduction in contrast for Gap OD > 0.25 . Note, with the proper orientation of linearly polarized light this effect could be potentially suppressed, since dipoles don't radiate along their axis of oscillation, although this has not been explored.

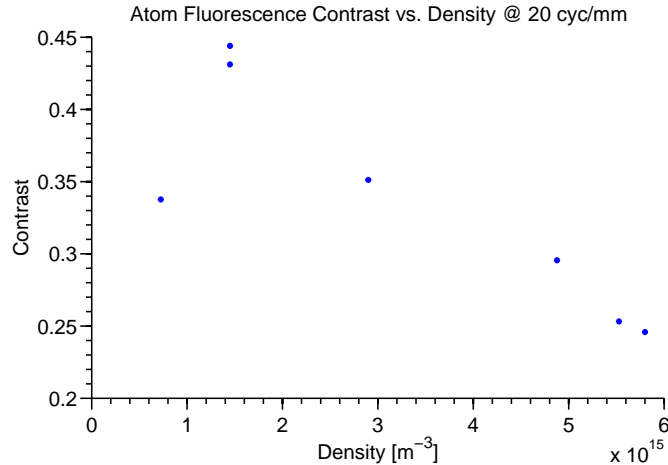


Figure 4.6 : The shown dependence on density for contrast of a 20 cyc/mm push beam modulation led to the exploration of optical depth effects

Since the ionizing beam excites to the continuum, the absorbed photons are not reemitted and this is not a concern for modulations of the 412 nm beam.

In conclusion, perhaps the decision of modulating the push beam or the ionizing beam should usually prefer the 412 nm beam. This avoids the mentioned contrast diminishing issues and with proper care, focused reflection related damage can be avoided with 412 nm modulations. It's worth noting, future plans of incorporating an electronically controlled spatial light modulator might limit the intensity of the modulated beam.

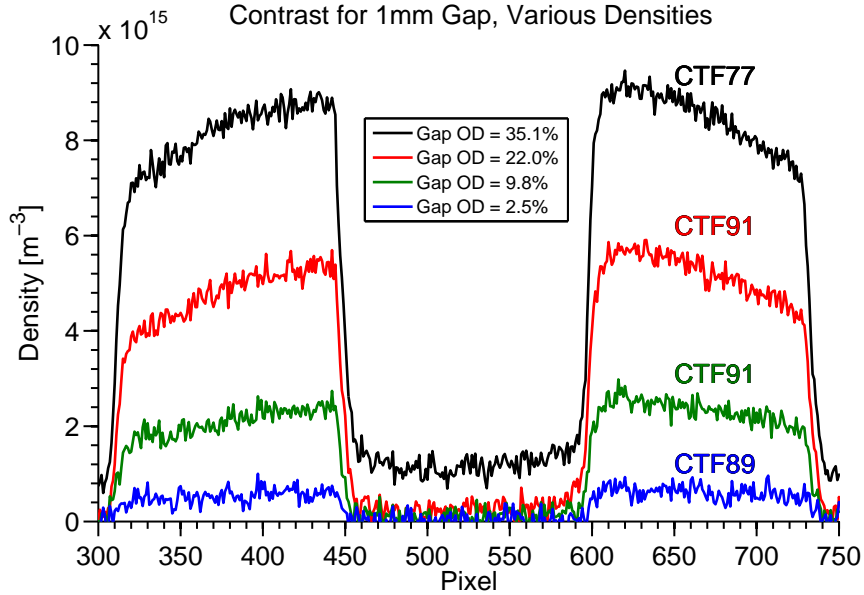


Figure 4.7 : Rescattered 461 nm light diminishes CTF, in optically thick clouds, by raising C_{min} over the entire cloud as well as a short transition region of decay at the edges of the gap. With a $\sigma_{abs} \approx 3.9 \times 10^{-14} \text{ m}^2$ the optical depth of the 1 mm gap is shown.

4.3 Total System Performance

To assess total system performance ultracold neutral plasmas were sculpted by modulating the ionizing beam with various spatial frequencies and ion fluorescence at 422 nm was imaged in order to measure CTFs, as shown in Figure 4.11. Some details of our fluorescence imaging are necessary before we continue. Due to the relatively narrow linewidth of our imaging laser ($\approx 7 \text{ MHz}$), ion spectra are broadened predominately by Doppler broadening. This means that any one detuning will be on resonance with a Doppler selected velocity group of ions and total plasma density is obtained by integrating several images taken across the resonance [51]. We will first discuss on-resonant results, then the effects of detuning the imaging beam. We will

show that reduced contrast in the total plasma density is due to plasma dynamics, which ultimately hinders the ability to image initial plasma density.

On-resonance imaging of sculpted UNPs is a good indicator of total system alignment and performance. It was found that 3 cyc/mm is a good frequency to use for rough alignment, and 5 cyc/mm for finer adjustment. Images were taken at 250 ns after plasma creation, limited by residual push beam fluorescence, due to slow turn off of push beam AOM. A gate-width of 500 ns was seen to not limit contrast for either frequency and gives sufficient SNR with ≈ 250 CCD accumulations. This means images are produced about one a minute, and can be used as "real-time" feedback. Best examples of each frequency are shown in Figures 4.8 and 4.9 and should be considered target when aligning the system.

We now explore the effect of detuning on measured contrast, more correctly, the lack of an effect. As shown in Figure 4.10, detuning of the image beam had little effect on measured contrast of a 5 cyc/mm modulation. By reviewing the series of images taken through the imaging resonance one sees a coherent wavefront for each Doppler selected velocity group, preserving the contrast of the original perturbation.

When all images in a scan across the imaging resonance are summed, the signal is proportional to the local plasma density. In these total density images (Figures 4.11 and 4.12) we see reduced contrast (compared to any individual image), which we attribute to plasma dynamics.

This can be seen by noting that normalized perturbation is shifted spatially as a function of detuning. As seen in Figure 4.13, left going ions are imaged slightly to the left of on resonance ions and right going ions are imaged to the right. When they are summed together, this leads to feature broadening and contrast is reduced.

The results of performance for 3 and 5 cyc/mm are summarized in Table 4.1.

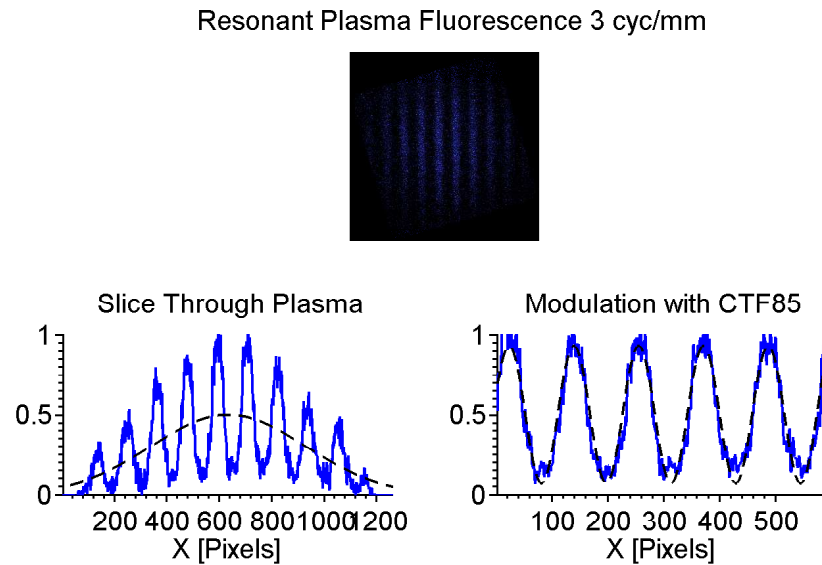


Figure 4.8 : CTF of 3 cyc/mm plasma modulations, imaged at 4X with 1x1 binning. This measurements represents system best for the conditions as described. Measurements are taken from 2D density images of the plasma (top). A central 1D cut of density (lower left, solid blue) is fit to a Gaussian profile (lower left, black dashed). Assuming the Ronchi pattern cuts ionization fraction in half (compared to a non perturbed plasma), allows normalization of the modulation (lower right, solid blue) by twice the fitted Gaussian and then a floating sin wave is fit (lower right, black dashed) to extract C_{Max} and C_{Min} .

While 4X magnification offers improvement for these spatial frequencies, it was seen that 10X magnification offers little additional improvement in resolution. This is reasonable since 3 cyc/mm magnified by 4X, is 0.75 cyc/mm and even the ICCD has near unity MTF at that frequency. At 5 cyc/mm, 4X magnification results in 1.25 cyc/mm, this is about when ICCD performance starts to plummet and hence 10X magnification offers marginal improvement for 5 cyc/mm. According to bench tests and seen in Figure 3.4, 10X should offer resolution benefits from 5-15 cyc/mm and

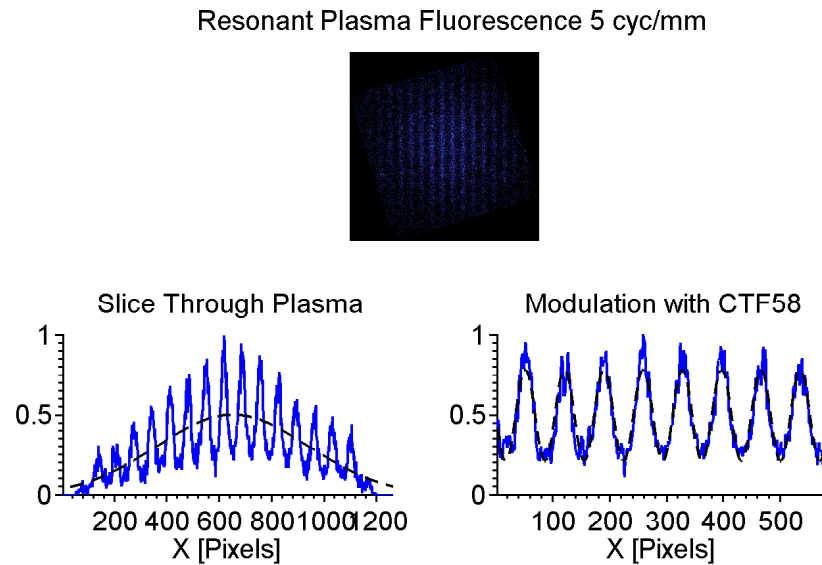


Figure 4.9 : CTF of 5 cyc/mm plasma modulations, imaged at 4X with 1x1 binning. This measurements represents system best for the conditions as described.

above 30 cyc/mm.

Unfortunately, we found that 5 cyc/mm was about the upper limit of initial plasma densities that can be imaged in real space. At 10 cyc/mm, we found it very difficult to achieve sufficient SNR for real time feedback and alignment, see Figure 4.14. We attribute this decreased optical performance, and plasma dynamics. Optical performance could be enhance with 10X magnification but it also dramatically decreases intensity (16% of that at 4X magnification) so that SNR is reduced even further. Camera gate width could be decreased to alleviate dynamic concerns but this too decreases SNR. To increase SNR, more CCD accumulations could be acquired, at a cost of image production rate or ccd pixels could be binned, however too much binning leads to resolution degradation. All this practically limits the ability to have quick feedback and hampers alignment. Working through these complications is beyond the scope of this work and will be one of the challenges for upcoming experiments.

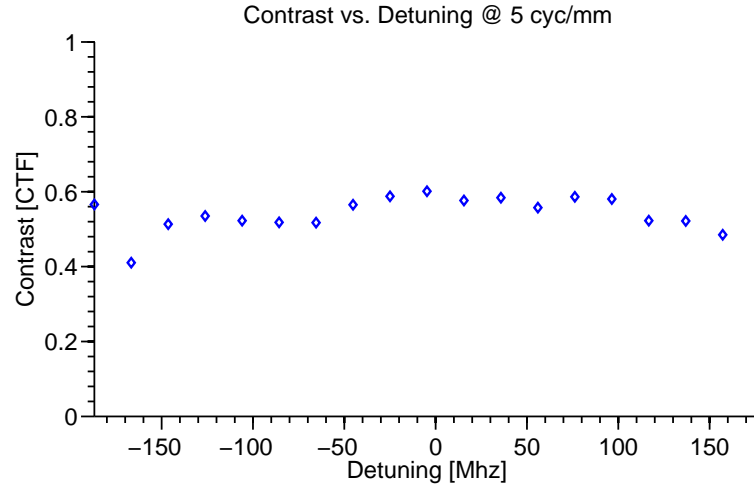


Figure 4.10 : CTF of 5 cyc/mm plasma modulations, imaged at 4X with 1x1 binning as a function of image beam detuning. Each detuning results in a consistent CTF that is higher than the CTF measured from total density images, see Figure 4.12. This can be interpreted as a spreading of the density features due to expansion of the plasma and the flat response indicates dynamics maintain spatial periodicity of the original modulation.

Table 4.1 : Modulated Plasma Imaging Performance Summary [On Resonance/-Summed Density]

Magnification	Spatial Frequency	
	3 cyc/mm	5 cyc/mm
1X	CTF60/CTF45	CTF45/CTF25
4X	CTF85/CTF68	CTF60/CTF33
10X	CTF85/CTF68	CTF65/CTF33

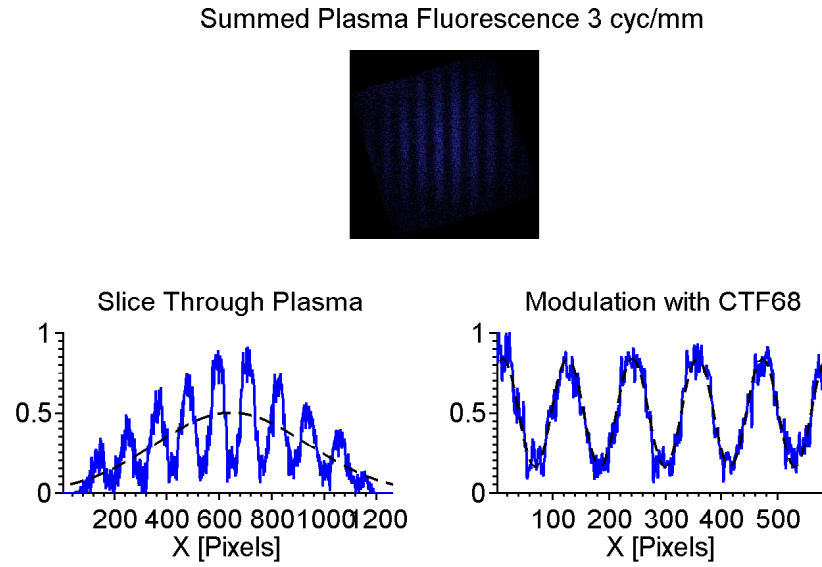


Figure 4.11 : Measuring CTF of 3 cyc/mm modulation, imaged with 4X imaging and 1x1 binning.

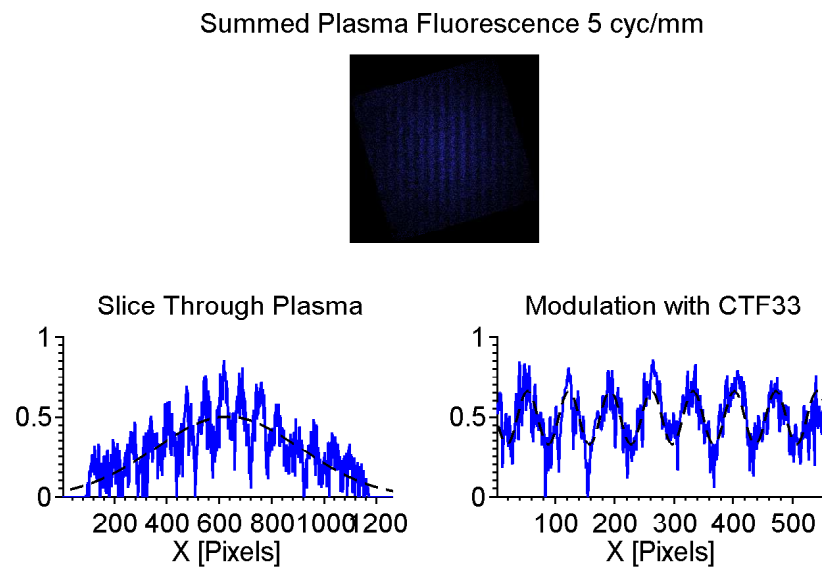


Figure 4.12 : Measuring CTF of 5 cyc/mm modulation, imaged with 4X imaging and 1x1 binning.

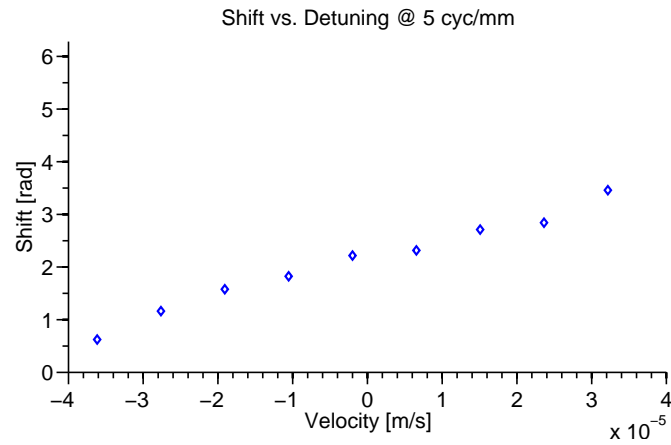


Figure 4.13 : By plotting the position of the fitted perturbation as a function of detuning, across a series of images taken through the resonance, one sees how total plasma density contrast is reduced when compared to individual or on-resonance images. Left going ions (indicated by negative detunings) are found to the left of stationary ions and right going ions to the right, indicating the spreading of density features and contrast reduction due to dynamics. Velocities (v) can be determined from laser detuning, through the Doppler relation, $\omega = v * k$, where ω is the detuning of the imaging laser and k is it's wave vector.

4.3.1 Velocity Space Analysis

The aforementioned complications encourage us to use other methods of analysis; instead of summing the images in frequency space and viewing them in real space, we can do just the opposite and we measure the velocity distribution of the ions. This has already been shown to be useful for analysing long wavelength IAWs [51] and should scale to smaller wavelengths. Preliminary review of velocity spectrum also hint at interesting dynamics as illustrated in the following paragraph.

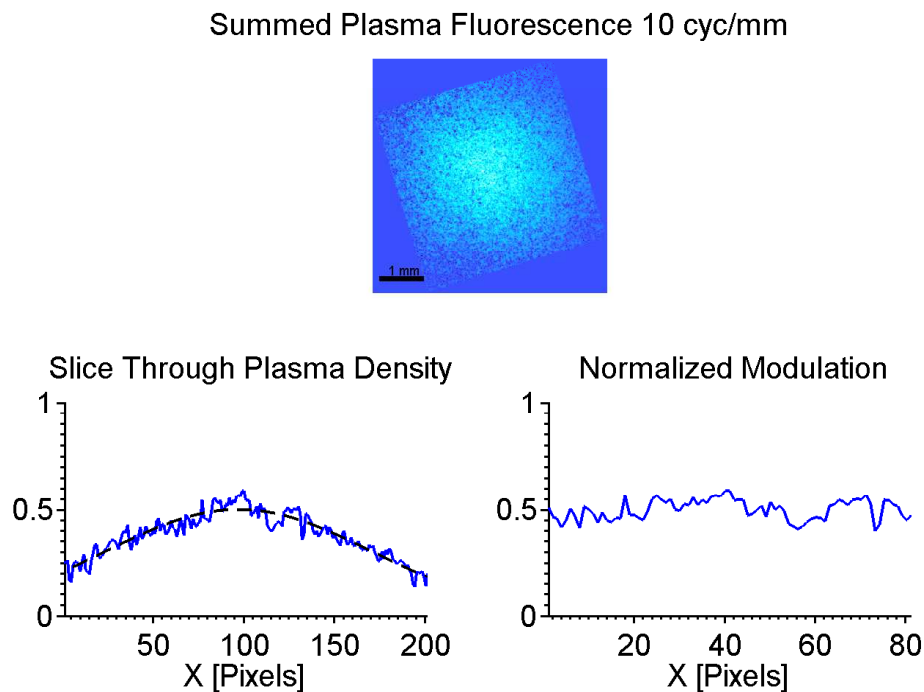


Figure 4.14 : At a spatial frequency of just 10 cyc/mm all contrast was lost within the first 500 ns. This complicates alignment and limits the ability to image initial plasma density in real time.

Comparing the velocity distributions of UNPs modulated at 3, 5 and 10 cyc/mm, we see signs of interesting dynamics, and hints explaining the lack of contrast at

10 cyc/mm. Specifically the increased broadening of the distribution for 10 cyc/mm indicates a larger average ion velocity, which indicates that dynamics are become more of a concern. The increased broadening makes sense when you consider hydrodynamic expansion of the plasma into a vacuum, which is driven by any gradient in the electron thermal pressure [29]. This could arise from a gradient in either temperature or density, but in this case it is the edge of each density feature that drives expansion into the voids of the modulation and reduces contrast. This would accelerate ions from a sheath approximately a Debye length thick and as the spatial frequency increases, this effects an increasing percentage of the total ions, although the gradient and hence the acceleration does not change with spatial frequency. This explains the relative line shapes, at 10 cyc/mm ions are not accelerated to higher velocities, that is the far wings aren't effected, however a larger fraction of ions are accelerated to intermediate velocities. For small enough features, i.e. when they are approx. two Debye lengths thick, all ions would be accelerated outward and contrast quickly diminished. For a typical Debye length of 10s of microns, this should happen around 10 cyc/mm and could very well explain our loss of contrast. To confirm this hypothesis an extensive study could be conducted by varying the Debye length and spatial frequency. On a side note broadening also decreases SNR for on-resonance images simply because there are fewer ions on resonance.

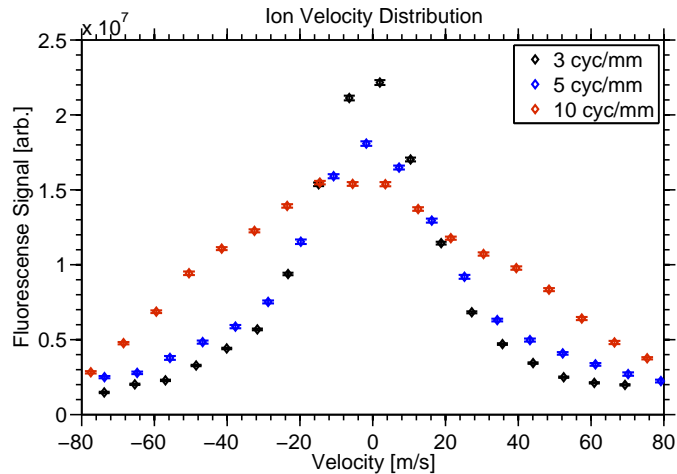


Figure 4.15 : Comparison of velocity distributions for 3, 5 and 10 cyc/mm modulated UNPS, taken at 500 ns after plasma creation. Notice an increase in spatial frequency changes the line shape, indicating acceleration of a larger fraction of ions, which reduces contrast. Velocities (v) are determined from laser detuning, through the Doppler relation, $\omega = v * k$, where ω is the detuning of the imaging laser and k is it's wave vector. Furthermore an ion with velocity of 60 m s^{-1} will move $30 \mu\text{m}$ in 500 ns and at 10 cyc/mm the gaps are only $50 \mu\text{m}$ wide. Since they are filling in from both sides, this is sufficient to explain the significant reduction of contrast.

4.4 Conclusion

In conclusion, high resolution relay optics were designed and implemented to sculpt ultracold neutral plasmas with length scales on the order of $10 \mu\text{m}$, over a large majority of the plasma cloud. Actual performance, specifically DOF, was better than predicted by simulations, probably due to the use of coherent laser light. These improvements access a new regime where feature sizes are on the order of the Debye length and many interesting deviations have been predicted, many of which probe strong coupling's effects. We also designed an imaging system capable of 50% con-

trast out to 100 cyc/mm. We found that the fast dynamics of small features present multiple challenges to accurately imaging the initial plasma density. Regardless the improved imaging resolution will increase regional analysis resolution and could answer a few open issues that possibly arise from spatial mixing of information. Beyond the many improvements we've already measured and seen, the full benefits of such a system are yet to be seen.

Appendix A

Labview Overhaul

Labview control programs for the UNP experiment were overhauled with an emphasis on user friendliness and error prevention. This was accomplished by taking the multitude of previously used VIs and integrating them into a single large control program, providing real time experimental control. Where possible, it includes state awareness and intelligently self manages to limit the possibility of human error.

Beyond the change to a true process flow type program, further improvements included drastic overhaul of front panel layout. Tabs were utilized to display only the pertinent indicators and controls based on the experimental state (i.e. Atom Absorption Live Images vs Ion Fluorescence Data Collection). All numbers were put into standard SI units to avoid errors of inputting values in the wrong units. Many unused ancillary calculations were removed, thus minimizing computational overhead.

Several minor features were added to facilitate day to day experimental needs. For example a column was added to the PulseBlaster (PB) array in order to reverse the polarity of a particular channel, XORed with the PB array, for channels with inverted logic. Another column was added to turn any particular channel on full time, ORed with PB Array. If both of these new columns are set for a particular channel then that channel is off at all times.

All non critical process were removed from the data collection process in order to minimize computational delays and improve reproducibility of experimental data.

The batch file for a data run was updated to be a complete record of experimental parameters, and headings were added to the raw text file for readability. Also a screenshot of the front panel is now stored with every data run, ensuring proper record of experimental parameters.

Upon starting the PlasmaExperiment.vi a series of tasks are accomplished to initialize the various input/output cards, the PulseBlaster timing generator, and the imaging camera. Also certain appropriate controls are set to the default state. Then the program enters a perpetual loop where it simply waits for a change to the front panel. Depending on the nature of the change, various process are handled in a case structure and the loop is repeated to wait for the next interaction. This structure scales simply to add new functionality and can be put on a timer to invoke periodic processes. In this waiting state the user might wish to generate live images, at the simple click of a button a control bit is sent to another loop that obtains, saves and analyzes (if desired) live images. If a control is adjusted while images are being collected, the program decides if image collection must be momentarily suspended to make the update. At the end of the day the user pushes the front panel "Shut Down" button and the collection of images is ceased (if necessary), all cards are stopped, resources are released, front panel values are saved as defaults and the program is stopped.

Appendix B

Matlab Standardization

B.1 Analysis Template

Now that the collection of experimental data and parameters has been fully automated and is complete, the usefulness of an analysis program template was evident. The template is simply a bare-bones program designed to efficiently read in data, backgrounds, batch files and all recorded experimental parameters. It also calculates commonly used values and sets several common variables. From this starting point, programs can be quick adapted to specific analysis needs. This provides a single place for the retention of best programming practices and continuous improvement of lab analysis techniques, that is, it avoids random copying and pasting of outdated code. The current template can be found at `\\Ytterbium\Analysis\Templates\`.

B.2 Matlab Defaults

Continuing the spirit of consistency and efficiency, default figure properties were added to `startup.m` to facilitate the production of consistent images and plots. The file follows and is easily expanded for future needs.

B.2.1 `startup.m`

```
ScreenSizeArray = get(0, 'ScreenSize'); %screen size  
set(0, ...
```

```

'DefaultFigurePosition',[ScreenSizeArray(3)/4
    ScreenSizeArray(4)/4 ScreenSizeArray(3)/2
    ScreenSizeArray(4)/2],... %center 1/4 area of screen
'DefaultFigurePaperPositionMode','auto',... %WYSIWYG when
    printing
'DefaultSurfaceEdgeColor','none',... %no edge coloring
    for surface plots
'DefaultAxesBox','off',...
'DefaultAxesXGrid','off',...
'DefaultAxesYGrid','off',...
'DefaultAxesZGrid','off',...
'DefaultAxesFontSize',20,...
'DefaultAxesLinewidth',1.5,...
'DefaultTextFontSize',20,...
'DefaultLineLinewidth',2,...
'DefaultAxesTickDir','out',...
'DefaultAxesTickLength',[.02 .02],...
'DefaultAxesXMinorTick','on',...
'DefaultAxesYMinorTick','on');

```

Appendix C

ESF - LSF Code

```
close all
clear all

ImageFilePath='C:\Data\09.22.11\';

EdgeImage=0;
NormImage=0;
BkgdImage=0;

%Read in image. Confirmed-averaging doesn't reduce MTF
for i=1:2
    ImageFileName=['edge' num2str(i) '.dat'];
    Image=dlmread([ImageFilePath ImageFileName]);
    EdgeImage=EdgeImage+Image;
end
EdgeImage=EdgeImage/i;

%Read in normalization image. Confirmed-averaging doesn't
reduce MTF
```

```

for i=1:2
    ImageFileName=['normal' num2str(i) '.dat'];
    Image=dlmread([ImageFilePath ImageFileName]);
    NormImage=NormImage+Image;
end

    NormImage=NormImage/i;

BkgdImageFileName='bkgd.dat';
BkgdImage=dlmread([ImageFilePath BkgdImageFileName]);
NormEdgeImage=(EdgeImage-BkgdImage)./(NormImage-BkgdImage); %
    subtracting BKGD and normalizing by intensity
NormEdgeImage=NormEdgeImage(470:530,:); %isolating center of
    field
[SizeY ,SizeX]=size(NormEdgeImage);

X=1:SizeX;
Y=1:SizeY;
XFine=1:0.05:SizeX; %subsampling grid of 1/20th a pixel

%for every row, find the location of the edge (50% intensity)
for k=Y
    IntEdge=interp1(NormEdgeImage(k,:),XFine,'cubic');
    XAbove=XFine(IntEdge>0.5);
    EdgeLocX(k)=XAbove(1);
end

```

```

%fit a line (the edge) to the locations calculated above
S=polyfit (EdgeLocX,Y,1);
Alpha=atan(1/abs(S(1))); %angle of edge, necessary for
    rescaling frequencies later
N=ceil(abs(S(1))); %number of rows before shifting one full
    pixel
NumOfSSESFs=floor(SizeY/N); %number of complete subsampled
    ESFs

%build the subsampled ESFs
for k=1:NumOfSSESFs;
    EdgeCut=NormEdgeImage(1+(k-1)*(N):N*k,:);
    ESF=EdgeCut(:,1);
        for l=2:size(EdgeCut,2)
            ESF=vertcat(ESF,EdgeCut(:,l));
        end
    ESF=ESF';
    SSESF(k,:)=ESF;
end

%find the edge in each of the ssESFs by a linear fit of
    30%-70% range
for k=1:NumOfSSESFs;
    X30=find(SSESF(k,:)>.3,1,'first');

```



```

X70=find (SSESF(k,:) <.7,1, 'last ');
S2=polyfit (X30:X70,SSESF(k,X30:X70),1);
LinearFit=polyval (S2,X30:X70);
X50=find (LinearFit >.5,1, 'first ');
SSEdgeLoc(k)=X30+X50-1;
end

%shift ssESFs so that edges are aligned
for k=1:NumOfSSESFs-1;
    Shift=SSEdgeLoc(k)-SSEdgeLoc(end);
    SSESF(k,:)=circshift (SSESF(k,:),[0,-Shift]);
end

CutWidth=SSEdgeLoc(1)-SSEdgeLoc(end); %calculate amount of
    wrapping of image due to shifting edges
ESF=mean(SSESF(:,1:end-CutWidth),1); %average ssESFs into one
    and cut off bad edge

ESF=ESF-mean(ESF(1:10),2); %ensure esf starts at zero
ESF=ESF./mean(ESF(end-10:end),2); %ensure ESF ends at 1

%calculated average of forward and reverse derivative
LSF=conv([- .5 0 .5],ESF);
LSF=-LSF(3:end-2);
LSF=LSF-(mean(LSF(1:300))+mean(LSF(end-300:end))); %remove
    any "offset" from LSF

```

```

[LSFMax LSFMaxInd]=max(LSF) ;
LSF=LSF(LSFMaxInd-1538:LSFMaxInd+1538); %limit to \pm 1 mm
from max, the extent of the psf, from direct measurement
%% Deviation from Bohn algorithm
LSF=LSF./sum(LSF); %normalize to unity area

M=size(LSF,2) ;
Window=hamming(M, 'periodic') ;
WindowedLSF=Window'.*LSF; %hamming window applied to limit "
leakage" in the FFT %% Deviation from Bohn algorithm
WindowedLSF=WindowedLSF./sum(WindowedLSF); %normalize to
unity area

figure(1)
colormap(gray(100));
subplot(2,2,1)
    pcolor(NormEdgeImage);
    title('Image of Edge');
    xlabel('X [pix]'); ylabel('Y [pix]');
subplot(2,2,2)
    pcolor(SSESF);
    title('Subsampled & Shifted Edges');
    xlabel('X [subpix]'); ylabel('SSESFs');
subplot(2,2,3)
    plot(ESF, 'o-b', 'LineWidth',3);

```

```

    title ( 'Average_L Measured_L ESF' );
    xlabel ( 'Position_L [subpix]' ); ylabel ( 'Intensity_L [arb.]' );
    grid on
    grid minor
    axis tight
subplot (2,2,4)
    hold on
    plot ( LSF ./ max ( LSF ), '*r', 'LineWidth', 3 );
    plot ( WindowedLSF ./ max ( WindowedLSF ), '*b', 'LineWidth', 3 );
    title ( 'Measured_L SF' );
    xlabel ( 'Position_L [subpix]' ); ylabel ( 'Intensity_L [arb.]' );
    grid on
    box on
    grid minor
    axis tight

```

```

PixelSize = 0.013; %in mm
Nyquist = floor ( 1 / ( 2 * PixelSize ) ); %calculate maximum freq for
    discrete sampling size (pixel limited resolution)
DX = PixelSize / ( N - 1 ); %pixel size divide by subsampling in mm
NFFT = 2 ^ nextpow2 ( M ); % Next power of 2 from length of y,
    allows speedy calculation of FFT
MIF = abs ( fft ( WindowedLSF, NFFT ) ); %Calculate MTF
Freqs = ( 0 : NFFT - 1 ) * ( 1 / ( DX * NFFT ) ); %Calculate frequency range
    of interest for calculated MTF

```

```

Freqs=Freqs./cos(Alpha); %correct frequencies for angle
MTF_Corr=sin(pi*DX*3*Freqs)./(pi*DX*3*Freqs);%%Correct for
    three point derivative
MIF(2:end) = MIF(2:end)./MTF_Corr(2:end); %%Apply correction

NyquistIndex=find(Freqs>Nyquist,1,'first'); %Cut off results
    just below Nyquist
MIF=MIF(1:NyquistIndex-1);
Freqs=Freqs(1:NyquistIndex-1);

figure(1000)
hold on
plot(Freqs,MIF,'o','MarkerSize',8);
title('CTF_calculated_from_SSESF_vs_Measured_CTF_Comparison
    (for_1X_Macro)');
xlabel('Frequency_(cyc/mm)');
ylabel('Contrast');
X=0:Nyquist;

%%Calculating CTF from MTF fit see Coltman formula 1954
CTF=zeros(1,Nyquist+1);
for i=X
    for j=1:4:Nyquist;
        CTF(i+1)=CTF(i+1)+interp1(Freqs,MIF,j*i,'cubic',0)/j -
            interp1(Freqs,MIF,(j+2)*i,'cubic',0)/(j+2); %%ok<AGROW
    end
end

```

```

        >
    end

end

CTF=4/pi*CTF;

plot(X,CTF, '-r', 'LineWidth', 3);

%Calculating Diffraction Limited MTF

Diam=37.5;

F=105;

Lambda=422E-6;

F_0=Diam/(F*Lambda);

DiffMTF=zeros(1, ceil(Freqs(end))+1);

for i=X

    DiffMTF(i+1)=DiffMTF(i+1)+(2/pi)*(acos(i/F_0)-(i/F_0)
        *(1-(i/F_0)^2)^.5);

end

plot(X,DiffMTF, '-b', 'LineWidth', 2);

%%Adding Data from Bench test

%%Coherent illumination with Macro lens and relay on bench

DataY =[66      54      52      58      56      56      54
        51      51      48      50      44      39      30
        28      21      19];

DataY=DataY./100;

```

```
DataX=[4.00      4.49  5.04  5.66  6.35  7.13  8.00  8.98  10.08
        11.31  12.70  14.25  17.96  20.16  22.63  25.40  28.51];
errorbar(DataX, DataY,0.05.*DataY,0*DataY, 'xk', 'MarkerSize'
        ,8);
xlim ([0 ,Nyquist ])
ylim ([0 ,1])
legend( 'MTF_from_SSESF', 'CTF_from_SSESF', 'Diffraction Limit',
        'Msrd_CTF');%
```

Bibliography

- [1] F. F. Chen, *Introduction to Plasma Physics*. Plenum, New York, 1974.
- [2] T. H. Stix, *Waves in Plasmas*. New York: AIP, 2nd ed., 1992.
- [3] S. Ichimuru, *Statistical Plasma Physics, Volume II: Condensed Plasmas*, vol. 2 of *Frontiers in Physics*. Boulder, CO: Westview Press, 2004.
- [4] S. Ichimuru, “Strongly coupled plasmas: high-density classical plasmas and degenerate electron liquids,” *Rev. Mod. Phys.*, vol. 54, no. 4, p. 1017, 1982.
- [5] M. Bonitz, C. Henning, and D. Block, “Complex plasmas: a laboratory for strong correlations,” *Reports on Progress in Physics*, vol. 73, no. 6, p. 066501, 2010.
- [6] J. Castro, P. McQuillen, H. Gao, and T. C. Killian, “The role of collisions and strong coupling in ultracold plasmas,” *Journal of Physics: Conference Series*, vol. 194, p. 012065, 2009.
- [7] P. K. Kaw, “Collective modes in a strongly coupled dusty plasma,” *Phys. Plasmas*, vol. 8, no. 5, p. 1870, 2001.
- [8] H. M. V. Horn and S. Ichimaru, “Strongly coupled plasma physics,” 1993.
- [9] G. Kalman, K. I. Golden, and M. Minella, “Correlational and strong coupling effects on collective modes in plasmas,” in *Strongly Coupled Plasma Physics* (H. M. V. Horn and S. Ichimaru, eds.), p. 323, University of Rochester Press, Rochester, 1993.

- [10] M. S. Murillo, “Strongly coupled plasma physics and high energy density matter,” *Phys. Plasmas*, vol. 11, p. 2964, 2004.
- [11] D. B. Melrose, *Instabilities in Space and Laboratory Plasmas*. Cambridge: Cambridge University Press, 1986.
- [12] Z. Donko and P. Hartmann, “Thermal conductivity of strongly coupled Yukawa liquids,” *Phys. Rev. E*, vol. 69, no. 1, p. 016405, 2004.
- [13] Z. Donko and P. Hartmann, “Shear viscosity of strongly coupled Yukawa liquids,” *Phys. Rev. E*, vol. 78, p. 026408, 2004.
- [14] K. Golden, G. Kalman, and P. Hammerling, “Beam-plasma instabilities in a strongly coupled plasma,” *Physics Letters A*, vol. 80, no. 2-3, pp. 149 – 152, 1980.
- [15] R. Redmer, “Strongly coupled plasmas,” in *Plasma Physics: Confinement, Transport, and Collective Effects* (A. Drinkage, T. Klinger, G. Marx, and L. Schweikhard, eds.), (Berlin), p. 117, Springer, 2005.
- [16] R. Blandford and K. Thorne, *Application of Classical Physics*. in preparation, <http://www.pma.caltech.edu/Courses/ph136/yr2008/0820.1.K.pdf>, 2010.
- [17] T. C. Killian, T. Pattard, T. Pohl, and J. M. Rost, “Ultracold neutral plasmas,” *Physics Reports*, vol. 449, p. 77, 2007.
- [18] T. C. Killian, “Ultracold neutral plasmas,” *Science*, vol. 316, p. 705, 2007.
- [19] Y. C. Chen, C. E. Simien, S. Laha, P. Gupta, Y. N. Martinez, P. G. Mickelson, S. B. Nagel, and T. C. Killian, “Electron screening and kinetic energy oscillations in a strongly coupled plasma,” *Physical Review Letters*, vol. 93, p. 265003, 2004.

- [20] C. E. Simien, Y. C. Chen, P. Gupta, S. Laha, Y. N. Martinez, P. G. Mickelson, S. B. Nagel, and T. C. Killian, “Using absorption imaging to study ion dynamics in an ultracold neutral plasma,” *Physical Review Letters*, vol. 92, no. 14, p. 143001, 2004.
- [21] E. A. Cummings, J. E. Daily, D. S. Durfee, and S. D. Bergeson, “Fluorescence measurements of expanding strongly-coupled neutral plasmas,” *Physical Review Letters*, vol. 95, p. 235001, 2005.
- [22] T. C. Killian, Y. C. Chen, P. Gupta, S. Laha, Y. N. Martinez, P. G. Mickelson, S. B. Nagel, A. D. Saenz, and C. E. Simien, “Absorption imaging and spectroscopy of ultracold neutral plasmas,” *Journal of Physics B: Atomic, Molecular and Optical Physics*, vol. 38, p. 351, 2005. (Equations 7, 10, 11, and 17 should be multiplied by γ_0/γ_{eff}).
- [23] J. Castro, H. Gao, and T. C. Killian, “Using sheet fluorescence to probe ion dynamics in an ultracold neutral plasma,” *Plasma Phys. Control. Fusion*, vol. 50, p. 124011, 2008.
- [24] D. S. Bethune, “Dye cell design for high-power low-divergence excimer-pumped dye lasers,” *Appl. Opt.*, vol. 20, pp. 1897–1899, Jun 1981.
- [25] J. Castro, P. McQuillen, and T. C. Killian, “Ion acoustic waves in ultracold neutral plasmas,” *Physical Review Letters*, vol. 105, p. 065004, 2010.
- [26] D. Malacara and B. J. Thompson, *Handbook of Optical Engineering*. New York: Marcel Dekker, Inc., 2001.
- [27] T. Pohl and T. Pattard, “Strong-coupling effects in the relaxation dynamics of ultracold neutral plasmas,” *J. Phys. Conf. Series*, vol. 11, p. 223, 2005.

- [28] V. F. Kovalev and V. Y. Bychenkov, “Analytic solutions to the Vlasov equations for expanding plasmas,” *Physical Review Letters*, vol. 90, no. 18, p. 185004, 2003.
- [29] S. Laha, P. Gupta, C. E. Simien, H. Gao, J. Castro, and T. C. Killian, “Experimental realization of an exact solution to the Vlasov equations for an expanding plasma,” *Physical Review Letters*, vol. 99, p. 155001, 2007.
- [30] P. McQuillen, J. Castro, and T. C. Killian, “High-resolution ionization of ultra-cold neutral plasmas,” *J. Phys. B*, vol. 44, p. 184013, 2011.
- [31] N. Sato, H. Ikezi, N. Takahashi, and Y. Yamashita, “Large-amplitude ion acoustic waves in a plasma,” *Phys. Rev.*, vol. 183, pp. 278–287, Jul 1969.
- [32] F. Robicheaux and J. D. Hanson, “Simulated expansion of an ultra-cold, neutral plasma,” *Phys. Plasmas*, vol. 10, no. 6, p. 2217, 2003.
- [33] Y. Nakamura, H. Bailung, and P. K. Shukla, “Observation of ion-acoustic shocks in a dusty plasma,” *Physical Review Letters*, vol. 83, no. 8, p. 1602, 1999.
- [34] J. C. Feltz and M. A. Karim, “Modulation transfer function of charge-coupled devices,” *Appl. Opt.*, vol. 29, p. 712, 1990.
- [35] O. H. Schade, “Electro-optical characteristics of television systems,” *Radio Corporation of America*, vol. 9, p. 246, 1948.
- [36] J. W. Coltman, “The specification of imaging properties by response to a sine wave input,” *J. Opt. Soc. Am.*, vol. 44, p. 468, 1954.
- [37] E. Hecht, *Optics*. Addison-Wesley, 2002.
- [38] I. Csorba, *Image tubes*. Howard W. Sams engineering-reference book series, H.W. Sams, 1985.

- [39] M. Bass, *Handbook of Optics*. McGraw-Hill.
- [40] A. Frenkel, M. A. Sartor, and M. S. Wlodawski, "Photon-noise-limited operation of intensified CCD cameras," *Appl. Opt.*, vol. 36, pp. 5288–5297, Aug 1997.
- [41] L. A. Bosch, "Image intensifier tube performance is what matters," in *Image Intensifiers and Applications II* (C. B. Johnson, ed.), pp. 65–78, SPIE, 2000.
- [42] P. Colarusso and K. R. Spring, "Imaging at low light levels with cooled and intensified charge-coupled device cameras," in *Biophotonics, Part A* (I. P. Gerard Marriott, ed.), vol. 360 of *Methods in Enzymology*, pp. 383 – 394, Academic Press, 2003.
- [43] E. Buhr, S. Gnther-Kohfahlb, and U. Neitzelb, "Simple method for modulation transfer function determination of digital imaging detectors from edge images," *Proc. SPIE*, vol. 5030, 2003.
- [44] E. Buhr, S. Gnther-Kohfahlb, and U. Neitzelb, "Accuracy of a simple method for deriving the presampled MTF of a digital radiographic system from an edge image," *Med. Phys.*, vol. 30, 2003.
- [45] E. Samei, E. Buhr, P. Granfors, D. Vandembroucke, and X. Wang⁵, "Comparison of edge analysis techniques for the determination of the MTF of digital radiographic systems," *Phys. Med. Biol.*, vol. 50, 2005.
- [46] G. D. Boreman and S. Yang, "Modulation transfer function measurement using three- and four-bar targets," *Appl. Opt.*, vol. 34, p. 8050, 1995.
- [47] G. D. Boreman, *Modulation transfer function in optical and electro-optical systems*. Washington: SPIE Press, 2001.

- [48] C. E. Burkhardt, J. L. Libbert, J. Xu, J. J. Leventhal, and J. D. Kelley, “Absolute measurement of photoionization cross sections of excited atoms: Application to determination of atomic beam densities,” *Phys. Rev. A*, vol. 38, pp. 5949–5952, Dec 1988.
- [49] W. Mende, K. Bartschat, and M. Koch, “Near-threshold photoionization from the Sr I ($5s5p$) $^1P_1^o$ state,” *Journal of Physics B: Atomic, Molecular and Optical Physics*, vol. 28, no. 12, p. 2385, 1995.
- [50] C. Foot, *Atomic Physics*. Oxford master series in physics, Oxford University Press, 2005.
- [51] T. C. Killian, P. McQuillen, T. M. O’Neil, and J. Castro, “Creating and studying ion acoustic waves in ultracold neutral plasmas,” *ArXiv e-prints*, Jan. 2012.